MICRO-COMPUTER NETWORK ARCHITECTURE FOR RANGE INSTRUMENTATION APPLICATIONS

Final Report

(Contract DAAD07-87-C-0103)

September 16, 1987 through March 13, 1988

Prepared for

Commander
U.S. Army White Sands Missile Range
STEWS-ID-T
White Sands Missile Range, NM 88002

Prepared by

M.R. Belzer, Y.M. Cho

Mentor Technologies, Inc.
53-50 206th Street
Bayside, New York 11364

March 13, 1988

"The views, opinions, and findings contained in this report are those of the author(s) and should not be construed as an official Department of the Army position, policy or decision, unless so designated by other documentation."

SECURITY CLASSIFICATION OF THIS PAGE

REPORT DOCUMENTATION PAGE

Form Approved OMB No. 0704-0188

1a. REPORT SECURITY CLASSIFICATION: unclassified	1b. RESTRICTIVE MARKINGS
2a. SECURITY CLASSIFICATION AUTHORITY	3. DISTRIBUTION/AVAILABILITY OF REPORT: approved for public release; distribution is unlimited.
2b. DECLASSIFICATION/DOWNGRADING SCHEDULE	
4. PERFORMING ORGANIZATION REPORT NUMBER(S)	5. MONITORING ORGANIZATION REPORT NUMBER(S)
6a. NAME OF PERFORMING ORGANIZATION: Mentor Technologies, Inc. / 6b. OFFICE SYMBOL (If applicable)	7a. NAME OF MONITORING ORGANIZATION: U.S. Army White Sands Missile Range
6c. ADDRESS (City, State, and ZIP Code): 53-50 206th Street, Bayside, New York 11364	7b. ADDRESS (City, State, and ZIP Code): Commanding Officer, STEWS-ID-T, U.S. Army White Sands Missile Range, New Mexico 88002-5143
8a. NAME OF FUNDING/SPONSORING ORGANIZATION / 8b. OFFICE SYMBOL (If applicable)	9. PROCUREMENT INSTRUMENT IDENTIFICATION NUMBER: DAAD07-87-C-0103
8c. ADDRESS (City, State, and ZIP Code)	10. SOURCE OF FUNDING NUMBERS: PROGRAM ELEMENT NO. 665502 / PROJECT NO. 1P65502 M40 / TASK NO. / WORK UNIT ACCESSION NO.

11. TITLE (Include Security Classification)
Micro-Computer Network Architecture for Range Instrumentation Applications

12. PERSONAL AUTHOR(S)
M.R. Belzer, Y.M. Cho

13a. TYPE OF REPORT	13b. TIME COVERED	14. DATE OF REPORT (Year, Month, Day)	15. PAGE COUNT
Final Technical	FROM 16Sep87 TO 15Mar88	88 March 13	58

16. SUPPLEMENTARY NOTATION

17. COSATI CODES			18. SUBJECT TERMS (Continue on reverse if necessary and identify by block number)
FIELD	GROUP	SUB-GROUP	integrated tracking; decentralized estimation;

19. ABSTRACT (Continue on reverse if necessary and identify by block number)

VLSI technology has been developed to the point where special purpose processors may be concatenated to form supercomputers with far greater throughput rates than uniprocessor machines. MTI has developed a parallel form of the conventional Kalman filter that is well suited to being implemented in a multiprocessing environment. Moreover, our Decentralized Square Root Information Filter (DSRIF) has several very unique features which could be incorporated into the design of an integrated test range tracking system with much improved performance over existing methods.

Phase I research demonstrated feasibility of the DSRIF as a means for solving the linear least squares estimation problem in decentralized form. Also, an extended form of the DSRIF was derived and successfully used to track real Multiple Rocket Launch System Data provided by the White Sands Missile Range.

20. DISTRIBUTION/AVAILABILITY OF ABSTRACT	21. ABSTRACT SECURITY CLASSIFICATION
☒ UNCLASSIFIED/UNLIMITED ☐ SAME AS RPT. ☐ DTIC USERS	unclassified
22a. NAME OF RESPONSIBLE INDIVIDUAL: Foo Lam	22b. TELEPHONE (Include Area Code): (505)678-3010 / 22c. OFFICE SYMBOL: STEWS-ID-T

DD Form 1473, JUN 86 — Previous editions are obsolete. — SECURITY CLASSIFICATION OF THIS PAGE

MICRO-COMPUTER NETWORK ARCHITECTURE
FOR RANGE INSTRUMENTATION APPLICATIONS

Project Summary

Very Large Scale Integration (VLSI) technology has been developed to the point where special purpose processors may be concatenated to form supercomputers with far greater throughput rates than uniprocessor machines. MTI has developed a parallel form of the conventional Kalman filter that is well suited to being implemented in a multiprocessing environment. Moreover, our Decentralized Square Root Information Filter (DSRIF) has several very unique features which could be incorporated into the design of an integrated test range tracking system with much improved performance over existing methods.

Phase I research demonstrated feasibility of the DSRIF as a means for solving the linear least squares estimation problem in decentralized form. Also, an extended form of the DSRIF was derived and successfully used to process real Multiple Rocket Launch System Data provided by the White Sands Missile Range.

TABLE OF CONTENTS

	page
Cover Page	1
Report Documentation Page	2
Project Summary	3
List of Symbols	5
List of Figures	8
List of Tables	10
1.0 Introduction	11
2.0 Results of the Phase I Work	12
2.1 Derivation of the Decentralized Square Root Information Filter (DSRIF)	14
2.2 Validation of the DSRIF for a Simulated Ballistic Trajectory Over the White Sands Missile Range	18
2.3 Extended-Decentralized Square Root Information Filtering of MLRS Data	36
3.0 Estimates of Technical Feasibility	56
References	58

LIST OF SYMBOLS

i	superscripted local system number
j	superscripted vector element number
k	time index, may be subscripted or enclosed in parentheses
x_k	global state vector
w_k	global process noise vector
Φ_k	global state transition matrix
x_k^i	local state vector
${}_o x^i$	origin of a local coordinate system in earth centered earth fixed coordinates
${}_o x$	origin of the global coordinate system in earth centered earth fixed coordinates
${}_o r^i$	radial vector from earth's center to the origin of a local coordinate system
w_k^i	local process noise vector
Φ_k^i	local state transition matrix
y_k^i	local measurement vector
C_k^i	global observation sub-matrix
H_k^i	local observation matrix
v_k^i	local measurement noise vector
$x_k(\pm)$	$\begin{pmatrix}\text{measurement updated}\\ \text{time updated}\end{pmatrix}$ global state estimate
$x_k^i(\pm)$	$\begin{pmatrix}\text{measurement updated}\\ \text{time updated}\end{pmatrix}$ local state estimate
$P_k(\pm)$	$\begin{pmatrix}\text{measurement updated}\\ \text{time updated}\end{pmatrix}$ global estimate error covariance matrix
$P_k^i(\pm)$	$\begin{pmatrix}\text{measurement updated}\\ \text{time updated}\end{pmatrix}$ local estimate error covariance matrix
M_k^i	matrix of zeros and ones which partition the global states to the local systems
Q_k	covariance matrix for process noise vector

R_k^i covariance matrix for local measurement noise vector

$P_0(-)$ initial global estimate error covariance matrix

N number of time samples

M number of local systems

M^i number of local measurement variables

$z_w(k)$ "pseudomeasurement" vector

$R_w(k)$ inverse square root of Q_k

$R_k(\pm)$ (measurement updated / time updated) global square root information matrix

$z_k(\pm)$ (measurement updated / time updated) global square root information vector

$R_k^i(\pm)$ (measurement updated / time updated) local square root information matrix

$z_k^i(\pm)$ (measurement updated / time updated) local square root information vector

e_k^i local "innovations" vector

$R_w^{*(i)}(k)$ $R_{wx}^{*(i)}(k)$ $z_w^{*(i)}(k)$ local smoothing coefficients

$R_w^*(k)$ $R_{wx}^*(k)$ $z_w^*(k)$ global smoothing coefficients

$z^*(k)$ $H^*(k)$ merge coefficients

t continuous time variable

d^i local coordinate system displacement vector

L latitude of global coordinate system origin

δ longitude of global coordinate system origin

α^i
β^i Euler angles defining the orientation of the local coordinate system
τ^i w.r.t. to the global coordinate system

r_e average earth radius

${}^1T_k^i$ orthogonal transformation in local measurement update

${}^2T_k^i$ orthogonal transformation in local time update

$^{3}T_k$ orthogonal transformation in first merge step

$^{4}T_k$ orthogonal transformation in second merge step

$^{5}T_k^i$ orthogonal transformation in local measurement update (E-DSRIF)

$^{6}T_k^i$ orthogonal transformation in local time update (E-DSRIF)

T^i orthogonal coordinate transformation between the local and global coordinate system

T^g orthogonal coordinate transformation between the global coordinate system and the earth centered earth fixed coordinate system

μ product of G and re

r_k^i range measurement

$\dot{r}_k^i$ range rate measurement

θ_k^i elevation angle measurement

Γ_k^i azimuth angle measurement

G gravitational constant

m_e earth's mass

Ω earth's angular velocity

u(t) deterministic control

f(x(t),u(t)) nonlinear dynamics vector

$h^i(x(t))$ nonlinear local observation vector

F_k linearized dynamics matrix

LIST OF FIGURES

Figure 1: The Local Coordinate System and Measurement Variables.

Figure 2: Nominal Position Versus Time for the Ballistic Target.

Figure 3: Nominal Velocities Versus Time for the Ballistic Target.

Figure 4: Sensor #1 Azimuth and Elevation Measurements Corresponding to the Nominal Ballistic Trajectory.

Figure 5: Sensor #2 Azimuth and Elevation Measurements Corresponding to the Nominal Ballistic Trajectory.

Figure 6: Sensor #3 Range, Azimuth and Elevation Measurements Corresponding to the Nominal Ballistic Trajectory.

Figure 7: Sensor #4 Azimuth and Elevation Measurements Corresponding to the Nominal Ballistic Trajectory.

Figure 8: Sensor #5 Range, Azimuth and Elevation Measurements Corresponding to the Nominal Ballistic Trajectory.

Figure 9: Perturbed State Positions Versus Time for the Ballistic Target.

Figure 10: Perturbed State Velocities Versus Time for the Ballistic Target.

Figure 11: RMS Global Position Estimate Error Versus Time.

Figure 12: RMS Global Velocity Estimate Error Versus Time.

Figure 13: Global Position and Velocity Estimate Error Covariances Versus Time. $R_k(j,j)=10^{-5}$ for angle variables and 10^2 for range variables. $Q_k(j,j) = .1$ for all $j=1,\ldots,6$.

Figure 14: Global Position and Velocity Estimate Error Covariances Versus Time. $R_k(j,j)=10^{-5}$ for angle variables and 10^2 for range variables. $Q_k(j,j) = 1.$ for all $j=1,\ldots,6$.

Figure 15: Global Position and Velocity Estimate Error Covariances Versus Time. $R_k(j,j)=5 \times 10^{-5}$ for angle variables and 5×10^2 for range variables. $Q_k(j,j) = .1$ for all $j=1,\ldots,6$.

Figure 16: Radar #350 Range, Azimuth and Elevation Measurements for MLRS.

Figure 17: Radar #393 Range, Azimuth and Elevation Measurements for MLRS.

Figure 18: Radar #394 Range, Azimuth and Elevation Measurements for MLRS.

Figure 19: G30 Azimuth and Elevation Measurements for MLRS.

Figure 20: G80 Azimuth and Elevation Measurements for MLRS.

Figure 21: G106 Azimuth and Elevation Measurements for MLRS.

Figure 22: G110 Azimuth and Elevation Measurements for MLRS.

Figure 23: G152 Azimuth and Elevation Measurements for MLRS.

Figure 24: G220 Azimuth and Elevation Measurements for MLRS.

Figure 25: G254 Azimuth and Elevation Measurements for MLRS.

Figure 26: G256 Azimuth and Elevation Measurements for MLRS.

Figure 27: Derived Position Measurements from Radar #350.

Figure 28: Derived Velocity Measurements from Radar #350.

Figure 29: Derived Acceleration Measurements from Radar #350.

Figure 30: Derived Jerk Measurements from Radar #350.

Figure 31: Radar #350 Range, Azimuth and Elevation Estimates for MLRS.
$R_k(j,j)=10^{10}$ for ot variables and 10.,1.,1. for rt range, azimuth and elevation variables respectively.
$Q_k(j,j) =$ diag [1.7×10^{17} 7.4×10^{17} 9.3×10^{17}] .

Figure 32: Radar #394 Range, Azimuth and Elevation Estimates for MLRS.
$R_k(j,j)=10^{10}$ for ot variables and 10.,1.,1. for rt range, azimuth and elevation variables respectively.
$Q_k(j,j) =$ diag [1.7×10^{17} 7.4×10^{17} 9.3×10^{17}] .

Figure 33: G30 Azimuth and Elevation Estimates for MLRS.
$R_k(j,j)=10^{10}$ for ot variables and 10.,1.,1. for rt range, azimuth and elevation variables respectively.
$Q_k(j,j) =$ diag [1.7×10^{17} 7.4×10^{17} 9.3×10^{17}] .

Figure 34: G80 Azimuth and Elevation Estimates for MLRS.
$R_k(j,j)=10^{10}$ for ot variables and 10.,1.,1. for rt range, azimuth and elevation variables respectively.
$Q_k(j,j) =$ diag [1.7×10^{17} 7.4×10^{17} 9.3×10^{17}] .

Figure 35: G110 Azimuth and Elevation Estimates for MLRS.
$R_k(j,j)=10^{10}$ for ot variables and 10.,1.,1. for rt range, azimuth and elevation variables respectively.
$Q_k(j,j) =$ diag [1.7×10^{17} 7.4×10^{17} 9.3×10^{17}] .

Figure 36: Global Position Estimates (w.r.t. launch) Versus Time for MLRS.
$R_k(j,j)=10^{10}$ for ot variables and 10.,1.,1. for rt range, azimuth and elevation variables respectively.
$Q_k(j,j) =$ diag [1.7×10^{17} 7.4×10^{17} 9.3×10^{17}] .

Figure 37: Global Position Estimate Error Covariances Versus Time for MLRS.
$R_k(j,j)=10^{10}$ for ot variables and 10.,1.,1. for rt range, azimuth and elevation variables respectively.
$Q_k(j,j) =$ diag [1.7×10^{17} 7.4×10^{17} 9.3×10^{17}] .

LIST OF TABLES

Table 1: Optical Tracker (ot) and Range Radar (rr) Locations and Orientations in GCS for the Ballistic Target.

Table 2: Nominal Positions and Velocities for Key Time Points of the Ballistic Trajectory.

Table 3: Optical Tracker Locations and Orientations in GCS for the MLRS Tests.

Table 4: Radar Locations and Orientations in GCS for the MLRS Tests.

Table 5: Radar #350 and #394 Measurements and Estimated Measurements for MLRS. $R_k(j,j)=10^{10}$ for ot variables and 10.,1.,1. for rt range, azimuth and elevation variables respectively.
$Q_k(j,j)$ = diag [1.7×10^{17} 7.4×10^{17} 9.3×10^{17}] .

Table 6: G30, G80, G110 Measurements and Estimated Measurements for MLRS. $R_k(j,j)=10^{10}$ for ot variables and 10.,1.,1. for rt range, azimuth and elevation variables respectively.
$Q_k(j,j)$ = diag [1.7×10^{17} 7.4×10^{17} 9.3×10^{17}] .

Table 7: Global Position Estimates and Derived Measurements for MLRS. $R_k(j,j)=10^{10}$ for ot variables and 10.,1.,1. for rt range, azimuth and elevation variables respectively.
$Q_k(j,j)$ = diag [1.7×10^{17} 7.4×10^{17} 9.3×10^{17}] .

1.0 Introduction

VLSI (Very Large Scale Integration) technology has been developed to the point where high speed floating point processors may be concatenated to form compact supercomputers with far greater throughput than uniprocessor machines. Thus, there currently is considerable interest within the signal processing community in the development of parallel versions of many conventional algorithms such as convolution, matrix multiplication and factorization. MTI has collaborated with Dr. G.J. Bierman to develop a parallel form of the Kalman filter that has several very unique and important features. We believe that utilization of these features will result in the design of an integrated test range tracking system that exhibits much improved performance over the existing "independent" approach to tracking at the White Sands Missile Range (WSMR).

Specifically, our Decentralized Square Root Information Filter (DSRIF) [1] allows each group of measurement variables, the process noise statistics and the prior information about the initial state to be processed in separate but locally optimal filters. Globally optimal state estimates and estimate error covariances may then be computed by combining local filter outputs on demand. This will allow the analyst to identify the contribution of each measurement group, the process noise and the prior information about the initial state to the global state estimate and estimate error covariance without additional computation.

Furthermore, the process noise and prior information may be distributed amongst the data processing filters in order to improve upon the fault tolerant characteristics of the nominal algorithm when real-time signal processing is an issue. In this case, the estimates and covariances should gracefully degrade from global optimality as local processors fail. Thirdly, the algorithm is based upon numerically reliable matrix factorization methods which, unlike the Conventional Kalman Filter (CKF), will never fail.

The objective of Phase I research was to validate the DSRIF equations by testing its ability to track a predetermined ballistic trajectory when perturbed by white Gaussian noise. The state estimates and error covariances obtained were found to be identical (when printed to 10 significant digits) with those of a SRIF implemented in centralized form with all calculations performed in double precision arithmetic. Furthermore, an extended version of the DSRIF (E-DSRIF) was derived and successfully used to track real Multiple Rocket Launch System data obtained from the WSMR.

The remaining parts of this Phase I report are organized as follows. In the next section we formulate the decentralized estimation problem and define a necessary and sufficient condition for recovering globally optimal state estimates from locally optimal ones. Then, in section 2.1 we derive the DSRIF and show how the effects of prior and process noise may be distributed. In section 2.2, the ability of the DSRIF to accurately track the position and velocity of a ballistic object is tested via a computer simulation. Finally, in section 2.3, the E-DSRIF is used to track a maneuvering vehicle but using a polynomial process model for the target dynamics.

2.0 Results of the Phase I Work

The trajectory estimation problem is a problem of nonlinear estimation. Assume that the state of a target evolves in time according to the equation

$$\dot{x}(t) = f(x(t),u(t)) + w(t) \tag{1}$$

where u(t) is the target's nominal control vector and w(t) is a zero mean white noise process with spectral density Q(t). Values for the latter are selected in order to compensate for errors in the model which may originate from unknown perturbations to the nominal control (such as shear winds, wind gusting etc.) as well as from uncertainties in the aerodynamics of the target vehicle. The corresponding discrete measurement vector for the i^{th} sensor is given by

$$y_k^i = h^i(x_k) + v_k^i \tag{2}$$

where v_k^i is a zero mean white noise sequence with covariance R_k^i. The problem is to estimate the target states x_k based upon all of the past measurements y_l^i where ($1 \le i \le M$ and $1 \le l \le k$). The state vector x_k contains the target position and velocity, biases which account for the displacement and orientation of the sensor or "local" coordinate systems (LCSs) w.r.t. the global coordinate system (GCS), and acceleration when the target vehicle is maneuvering.

Unfortunately, the optimal nonlinear estimator (conditional mean) cannot be realized with a finite-dimensional implementation and consequently, all practical nonlinear filters must be suboptimal. The usual suboptimal solution is the CKF when the nominal trajectory is known a priori, the Extended Kalman Filter when the nominal trajectory is unavailable, and Higher Order Filters (such as the second order filter [4], the single-stage iterative filter [5], and the Gaussian sum filter [6], among others [7]) when even greater accuracy is desired. The tradeoff here is performance versus real-time computational requirement.

Thus, we see that the ability of a sensor group to accurately record the motion of one or more airborne targets is a function of the individual target and sensor dynamical models as well as the particular algorithm used to combine raw data and produce track estimates. Another issue is intersensor communication. Sensors which operate independently from one another will exhibit larger estimate errors than ones which communicate with other members of the network.

Let the global discrete time linear system

$$x_k = \Phi_{k-1}\, x_{k-1} + w_{k-1} \tag{3}$$

where

$$w_k = N(0,Q_k) \tag{4}$$

$$x_0 = N(0,P_0(-)) \tag{5}$$

be the model for the target, and the global measurement model

$$\begin{bmatrix} y_k^1 \\ \cdot \\ \cdot \\ \cdot \\ y_k^M \end{bmatrix} = \begin{bmatrix} C_k^1 \\ \cdot \\ \cdot \\ \cdot \\ C_k^M \end{bmatrix} x_k + \begin{bmatrix} v_k^1 \\ \cdot \\ \cdot \\ \cdot \\ v_k^M \end{bmatrix} \tag{6}$$

where v_k^1 through v_k^M are uncorrelated random vectors and

$$v_k^i = N(0, R_k^i) \tag{7}$$

be the model for the sensors.* The problem is to calculate the globally optimal (minimum mean square error) estimate of x_k and its associated estimate error covariance matrix P_k when y_k^1 through y_k^M are processed separately by locally optimal estimators 1 through M correspondingly. The local dynamical models are

$$x_k^i = \Phi_{k-1}^i \, x_{k-1}^i + w_{k-1}^i \tag{8}$$

where

$$w_k^i = N(0, Q_k^i) \tag{9}$$

$$x_0^i = N(0, P_0^i(-)) \tag{10}$$

and the local measurement models are

$$y_k^i = H_k^i \, x_k^i + v_k^i \tag{11}$$

where v_k^i satisfies (7). Notice that the local states may be physically different from the global states. Wilsky et.al. [3] have recently shown that a necessary and sufficient condition for our being able to recover globally optimal state estimates from locally optimal ones is that

$$C_k^i = H_k^i \, M_k^i \tag{12}$$

and for the tracking application, we expect that

$$x_k^i = M_k^i \, x_k \tag{13}$$

where M_k^i is a matrix which results in the correct partitioning of global states to the subsystem filters. Alternatively, equation (12) allows us to define the local state vector as d^i plus the local state vector defined in section 2.2 (both in local coordinates) provided that $M_k^i = (T^i)^{tr}$.

---

*Lower case variables are vector quantities while upper case generally corresponds to matrices of appropriate dimension. Also w_k, x_0, and v_k^1 through v_k^M are uncorrelated with each other for all k and N(a,B) signifies an a mean white Gaussian process with covariance matrix B.

2.1 Derivation of the DSRIF

The derivation of this algorithm may be found in our recent publication [1] with the exception of some new ideas on the distribution of prior information about the process (plant) noise and initial state amongst the local processors.

Let $M_k^i = I$. The goal is to find the sequence $x_0,\ldots,x_N$ that minimizes the least squares likelihood performance functional [2, pg.42]

$$J_N(x_0,\ldots,x_N) = || R_0(-)\, x_0 - z_0(-) ||^2 + \sum_{i=1}^{M} \sum_{k=0}^{N} ||(R_k^i)^{-\frac{1}{2}} H_k^i\, x_k - (R_k^i)^{-\frac{1}{2}} y_k^i||^2$$

$$+ \sum_{k=0}^{N-1} || z_w(k) - R_w(k)\, w_k ||^2 \qquad (14)$$

where the a priori estimate $R_0^{-1}(-)\, z_0(-)$ has covariance

$$P_0(-) = R_0^{-1}(-)\, R_0^{-T}(-)\,, \qquad (15)$$

$$Q_k = R_w^{-1}(k)\, R_w^{-T}(k)\,, \qquad (16)$$

$z_w(k) = R_w(k)$ times the a priori expectation of w_k, and the pair z_k^i, H_k^i correspond to normalized measurement equations i.e., $R_k^i = I$. Decentralized processing is achieved by distributing the minimization of the performance criterion amongst the local filters and global merging equations that follow. The best distribution for target tracking is probably to minimize $|| H_k^i\, xk - z_k^i ||^2$ in each of the M local filters and minimize the remaining two terms in (14) within the central (merge) processor. However, this point should be explored in detail in Phase II research. Thus, both data types may be processed using the standard SRIF mechanization:

Measurement Update

$${}^1T_k^i \begin{bmatrix} R_k^i(-) & z_k^i(-) \\ (R_k^i)^{-\frac{1}{2}} H_k^i & (R_k^i)^{-\frac{1}{2}} y_k^i \end{bmatrix} = \begin{bmatrix} R_k^i(+) & z_k^i(+) \\ 0 & e_k^i \end{bmatrix} \qquad (17)$$

Time Update

$${}^2T_k^i \begin{bmatrix} R_w(k) & 0 & z_w(k) \\ -R_k^i(+)\, \Phi_k^{-1} & R_k^i(+)\, \Phi_k^{-1} & z_k^i(+) \end{bmatrix}$$

$$= \begin{bmatrix} R_w^{*(i)}(k) & R_{wx}^{*(i)}(k) & z_w^{*(i)}(k) \\ 0 & R_{k+1}^{(i)}(-) & z_{k+1}^{(i)}(-) \end{bmatrix} \tag{18}$$

where

$$[\ R_0^i(-) \quad z_0^i(-)\ ] = [\ 0 \quad 0\ ] \tag{19}$$

$$[\ R_w(k) \quad z_w(k)\ ] = [\ 0 \quad 0\ ] \tag{20}$$

and ${}^1T_k^i$, ${}^2T_k^i$ are orthogonal transformations which put the matrices on the left hand sides of (17) and (18) into upper triangular form. They may be implicitly computed using Householder transformations [2, p.60-64].

In terms of the local filter results (17) and (18), the performance can be rewritten as

$$J_N(x_0,\ldots,x_N) = \| R_0(-)\, x_0 - z_0(-) \|^2 + \sum_{k=0}^{N-1} \| z_w(k) - R_w(k)\, w_k \|^2$$

$$+ \left\| \begin{bmatrix} R_w^{*(1)}(k) \\ \vdots \\ R_w^{*(M)}(k) \end{bmatrix} w_k + \begin{bmatrix} R_{wx}^{*(1)}(k) \\ \vdots \\ R_{wx}^{*(M)}(k) \end{bmatrix} x_{k+1} - \begin{bmatrix} z_w^{*(1)}(k) \\ \vdots \\ z_w^{*(M)}(k) \end{bmatrix} \right\|^2$$

$$+ \sum_{i=1}^{M} \sum_{k=0}^{M} \| e_k^{(i)} \|^2 + \left\| \begin{bmatrix} R_N^{(1)}(+) \\ \vdots \\ R_N^{(M)}(+) \end{bmatrix} x_N - \begin{bmatrix} z_N^{(1)}(+) \\ \vdots \\ z_N^{(M)}(+) \end{bmatrix} \right\|^2 \tag{21}$$

Applying an orthogonal transformation to the first three terms in (21), results in the following recursive equation for combining local smoothing coefficients with process noise and prior on x_0:

$$
{}^{3}T_k \begin{bmatrix} R_w^{*(1)}(k) & R_{wx}^{*(1)}(k) & z_w^{*(1)}(k) \\ \vdots & \vdots & \vdots \\ R_w^{*(M)}(k) & R_{wx}^{*(M)}(k) & z_w^{*(M)}(k) \\ R_w(k) & 0 & z_w(k) \\ -H^*(k-1)\,\Phi_k^{-1} & H^*(k-1)\,\Phi_k^{-1} & z^*(k-1) \end{bmatrix}
$$

$$
= \begin{bmatrix} R_w^*(k) & R_{wx}^*(k) & z_w^*(k) \\ 0 & H^*(k) & z^*(k) \\ 0 & 0 & \# \end{bmatrix} \tag{22}
$$

$$
\begin{bmatrix} H^*(-1) & z^*(-1) \end{bmatrix} = \begin{bmatrix} R_0(-) & z_0(-) \end{bmatrix} \tag{23}
$$

and $H^*(k)$ is upper triangular. To obtain the globally optimal information vector $z_k(+)$ and square root information matrix $R_k(+)$, we solve the following equations using $H^*(k)$ and $z^*(k)$ from (22):

$$
{}^{4}T_k \begin{bmatrix} R_k^{(1)}(+) & z_k^{(1)}(+) \\ \vdots & \vdots \\ R_k^{(M)}(+) & z_k^{(M)}(+) \\ H^*(k-1) & z^*(k-1) \end{bmatrix} = \begin{bmatrix} R_k(+) & z_k(+) \\ 0 & \# \end{bmatrix} \tag{24}
$$

where ${}^{4}T_k$ is an orthogonal transformation which puts the left hand side of (24) in upper triangular form. Globally optimal filter estimates and covariances are then given by

$$
x_k(+) = R_k^{-1}(+)\, z_k(+) \tag{25}
$$

$$
P_k(+) = R_k^{-1}(+)\, R_k^{-tr}(+) \tag{26}
$$

When the a priori information about the initial condition and process noise models are adjusted, it is only necessary to rerun (22) and (24) without reprocessing any measurements.

To summarize, each data-type is processed by a local SRIF

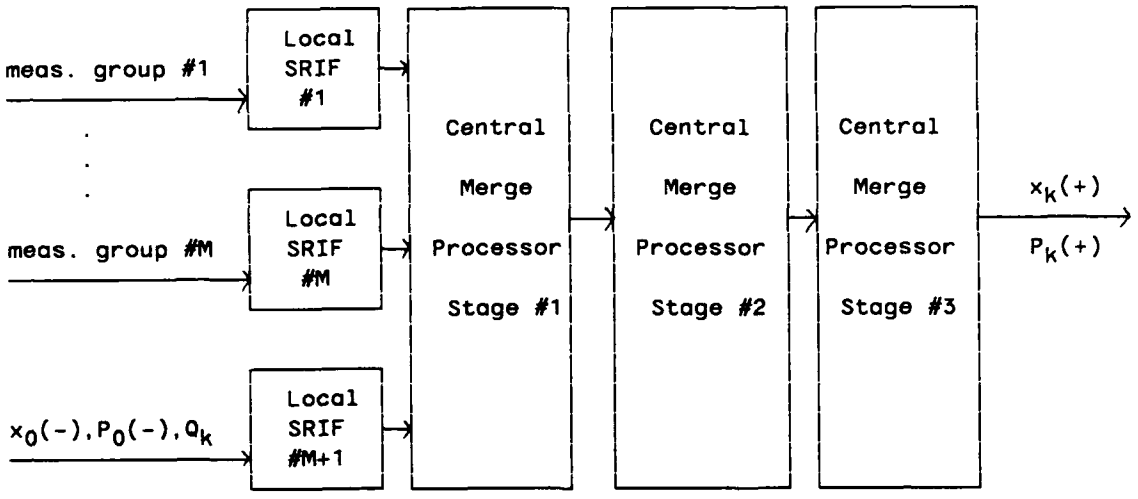

(17)-(20) which generates a set of smoothing coefficients $R_w^{*(i)}$, $R_{wx}^{*(i)}(+)$, $z_w^{*(i)}(+)$ as well as a square root information matrix $R(+)^{(i)}$ and information vector $z(+)^{(i)}$. The central or merge processor consists of three separate processors which operate in parallel. The first mechanizes (22),(23) which combines the local smoothing coefficients with the effects of process noise and prior information about the initial state. The second mechanizes (24) which merges the local square root information matrices and vectors with output from the first, but only upon demand by the third. The third produces estimates and covariances whenever desired by back-solving (25) and (26) respectively, noting that (25),(26) require output from the second processor. An important observation is that there is no feedback of information from the merge processor to the local filters.

Actually, a family of DSRIFs exist. Each member corresponds to a different distribution of process noise and prior information about the initial state amongst the local processors and the first merge processor (22),(23). To see this, realize that the prior and process noise terms in (14) may be written as

$$|| z_w(k) - R_w(k)\, w_k ||^2 = \sum_{i=1}^{M} || z_w(k)^{(i)} - R_w(k)^{(i)}\, w_k ||^2 \qquad (27)$$

$$|| R_0(-)\, x_0 - z_0(-) ||^2 = \sum_{i=1}^{M} || R_0(-)^{(i)}\, x_0 - z_0(-)^{(i)} ||^2 \qquad (28)$$

where the dimension of w and x are both n. The vectors $z_w(k)^{(i)}$, $z_0(-)^{(i)}$ and

matrices $R_w^{(i)}(k)$, $R_0^{(i)}(-)$ are chosen so that the local norms on the right hand side of (27),(28) remain invariant with respect to orthogonal transformations. Each norm may be incorporated into a local SRIF or the first merge processor and minimized there.

2.2 Validation of the DSRIF for a Simulated Ballistic Trajectory Over the White Sands Missile Range

In order to validate our decentralized approach to solving the linear least squares estimation problem, a high fidelity simulation of a multisensor network, tracking a ballistic trajectory over the WSMR, was encoded in Fortran '77 and executed on an IBM (clone) Model AT desktop computer (640K ram, 20 Mbyte hard disk, Intel 80287 math coprocessor). Initial conditions for the nominal trajectory were calculated using a "flat earth" or constant gravitational acceleration model which neglects the earth's rotation and assumes that the target vehicle is a point mass.

The initial position is launch complex #32 (E4,N2) and the desired terminal position is the GAM 83 target (E13,N85). This corresponds to a flight path of

$$((13-4)^2 + (85-2)^2)^{\frac{1}{2}} = 83.49 \text{ miles} \tag{29}$$

when projected onto the "Range Area - General Road Map (RAGRM)" which we use to define the GCS. That is x^1,x^2,x^3 is a right handed coordinate system where the vector cross product of x^1 with x^2 = x^3 and the vectors $[x^1\ 0\ 0]$ and $[0\ x^2\ 0]$ point east along latitude 32.380 degrees and north along longitude 106.481 degrees respectively. Then $[0\ 0\ x^3]$ is collinear with the radial vector which points outward from the earth's center and passes through the origin of the GCS. A launch elevation angle, w.r.t. the x^1,x^2 tangent plane, of 45 degrees was chosen in order to maximize the projected flight path for a given amount of energy. The corresponding initial positions and velocities are then

$$x_0^1 = 21{,}120. \text{ feet}$$

$$x_0^2 = 10{,}560. \text{ feet}$$

$$x_0^3 = 0. \text{ feet}$$

$$x_0^6 = ((32. \text{ feet/sec}^2)(83.49 \text{ miles}/2.)(5280 \text{ feet/mile}))^{\frac{1}{2}} = 2655.8 \text{ feet/sec} \tag{30}$$

$$x_0^4 = (x_0^6)(9./83.49) = 286.29 \text{ feet/sec}$$

$$x_0^5 = (x_0^6)(83./83.49) = 2640.21 \text{ feet/sec}$$

with a maximum ensuing altitude of

$$x^3(t_f/2.) = (x_0^6)^2/(2.(32. \text{ feet/sec}^2)) = 110{,}207. \text{ feet (20.9 miles)} \tag{31}$$

where

$$t_f = (83.49 \text{ miles})(5280 \text{ feet/mile})/x^6(0) = 165.99 \text{ seconds}, \quad (32)$$

the flight impact time.

Five sensor locations which cover both sides of the projected flight path were selected. They are Zebra (E3,N14), Rhodes Canyon Range Center (E0,N53), ABRES Radar (W10,N99), Oscura Range Center (E18,N77) and King I (E21,N34). Each sensor records measurements with respect to its own LCS so that coordinate transformations to the GCS were derived and included in the observational equations. The transformation is

$$\begin{bmatrix} x^1 \\ x^2 \\ x^3 \end{bmatrix} = (T^i) \begin{bmatrix} x^{i,1} \\ x^{i,2} \\ x^{i,3} \end{bmatrix} + d^i \quad (33)$$

where

$$T^i = ({}^8T^i) ({}^7T^i) ({}^6T^i) ({}^5T^i) \quad (34)$$

and

$${}^5T^i = \begin{bmatrix} 1 & 0 & 0 \\ 0 & \cos(L+\alpha^i) & \sin(L+\alpha^i) \\ 0 & -\sin(L+\alpha^i) & \cos(L+\alpha^i) \end{bmatrix} \quad (35)$$

$${}^6T^i = \begin{bmatrix} \cos\beta^i & 0 & -\sin\beta^i \\ 0 & 1 & 0 \\ \sin\beta^i & 0 & \cos\beta^i \end{bmatrix} \quad (36)$$

$${}^7T^i = \begin{bmatrix} 1 & 0 & 0 \\ 0 & \cos L & -\sin L \\ 0 & \sin L & \cos L \end{bmatrix} \quad (37)$$

$${}^8T^i = \begin{bmatrix} \cos\tau^i & \sin\tau^i & 0 \\ -\sin\tau^i & \cos\tau^i & 0 \\ 0 & 0 & 1 \end{bmatrix} \quad (38)$$

noting that $(T^i)^{tr} = (T^i)^{-1}$ since T^i is an orthogonal transformation. A computational savings results when $({}^5T^i)({}^6T^i)({}^7T^i)$ are combined using trigonometric identities for the cosine and sine of the sum of two angles along with the small angle approximation since α^i is bounded by $\pm$ 1 degrees over the length of the WSMR.

d^i Is the vector from the GCS to the ith LCS and $\alpha^i, \beta^i, \tau^i$ are the three Euler angles describing the orientation of the ith LCS w.r.t. the GCS. Specifically, if we first rotate about x^1 counterclockwise by an $(L+\alpha^i)$ degree change in latitude (aligning y^2 with the polar axis), and then rotate counterclockwise about y^2 by a β^i degree change in longitude, (β^i is bounded

by $\pm$ 1/2 degree over the width of the WSMR) then rotate clockwise about x3 by an L degree change in latitude, and finally rotate about z^4 by τ^i degrees to account for "tangent plane misalignment", the LCS will coincide with the GCS when $d^i = 0$. α^i Is equal to the LCS latitude - GCS latitude. β^i Is equal to the LCS longitude - GCS longitude.

To determine α^i, β^i given L, δ and d^i (in global coordinates), solve the following two equations:

$$\begin{bmatrix} {}^{o}x^{i,1} \\ {}^{o}x^{i,2} \\ {}^{o}x^{i,3} \end{bmatrix}_{ECEF} = \begin{bmatrix} {}^{o}x^{1} \\ {}^{o}x^{2} \\ {}^{o}x^{3} \end{bmatrix}_{ECEF} + T^{g} \begin{bmatrix} d^{i,1} \\ d^{i,2} \\ d^{i,3} \end{bmatrix}_{GCS} \tag{39}$$

where

$$\begin{bmatrix} {}^{o}x^{1} \\ {}^{o}x^{2} \\ {}^{o}x^{3} \end{bmatrix}_{ECEF} = \begin{bmatrix} r_e \cos L \cos \delta \\ -r_e \cos L \sin \delta \\ r_e \sin L \end{bmatrix} \tag{40}$$

and

$$T^{g} = \begin{bmatrix} \sin \delta & -\cos \delta & 0 \\ \cos \delta & \sin \delta & 0 \\ 0 & 0 & 1 \end{bmatrix} \begin{bmatrix} 1 & 0 & 0 \\ 0 & \sin L & -\cos L \\ 0 & \cos L & \sin L \end{bmatrix} \tag{41}$$

$$\begin{bmatrix} {}^{o}x^{i,1} \\ {}^{o}x^{i,2} \\ {}^{o}x^{i,3} \end{bmatrix}_{ECEF} = \begin{bmatrix} {}^{o}r^{i} \cos (L+\alpha^i) \cos (\delta+\beta^i) \\ {}^{o}r^{i} \cos (L+\alpha^i) \sin (\delta+\beta^i) \\ {}^{o}r^{i} \sin (L+\alpha^i) \end{bmatrix} \tag{42}$$

The solution is

$$L+\alpha^i = \tan^{-1} \frac{({}_{o}x^{i,3})^2}{({}_{o}x^{i,1})^2 + ({}_{o}x^{i,2})^2} \qquad (L+\alpha^i) \approx 32 \text{ degrees} \tag{43}$$

$$\delta+\beta^i = \cos^{-1} \frac{{}^{o}x^{i,1}}{{}^{o}r^{i} \cos (L+\alpha^i)} \qquad (\delta+\beta^i) \approx 106 \text{ degrees} \tag{44}$$

where

$${}^{o}r^{i} = \frac{{}^{o}x^{i,3}}{\sin (L+\alpha^i)} \tag{45}$$

The results are given in Table 1 below.

i	Sensor Type	$d^{i,1}$	$d^{i,2}$	$d^{i,3}$	$L+\alpha^i$	$\delta+\beta^i$	τ^i
1	ot	3.	14.	0.	32.5824	106.4295	0.
2	ot	0.	53.	0.	33.1462	106.4810	0.
3	rr	-10.	99.	0.	33.8109	106.6550	0.
4	ot	18.	77.	0.	33.4927	106.1690	0.
5	rr	21.	34.	0.	32.8710	106.1195	0.

Table 1: Optical Tracker (ot) and Range Radar (rr) Locations and Orientations in GCS for the Ballistic Target

Detailed equations that describe the translational motion of the target were developed. The equations include a radial gravitational force as well as centrifugal and Coriolis forces which come about by rotation of the GCS about the polar axis. The equations are

$$\dot{x}^4 = \frac{-\mu x^1}{((x^1)^2 + (x^2)^2 + (x^3+r_e)^2)^{3/2}} + 2\Omega(x^5 \sin L - x^6 \cos L) + \Omega^2 x^1 \qquad (46)$$

$$\dot{x}^5 = \frac{-\mu x^2}{((x^1)^2 + (x^2)^2 + (x^3+r_e)^2)^{3/2}} - 2\Omega x^4 \sin L + \Omega^2(x^2 \sin^2 L - (x^3+r_e)\cos L \sin L) \qquad (47)$$

$$\dot{x}^6 = \frac{-\mu(x^3+r_e)}{((x^1)^2 + (x^2)^2 + (x^3+r_e)^2)^{3/2}} + 2\Omega x^4 \cos L + \Omega^2((x^3+r_e)\cos^2 L - x^2 \cos L \sin L) \qquad (48)$$

where

$$\mu = G\, m_e \qquad (49)$$

and all other variables are defined in the List of Symbols. A spherical harmonic expansion of the earth's gravitational field is probably not necessary since most shots over the range are low altitude however, a major effect will be atmospheric drag and more precise modeling may be necessary.

Any one of three sensor types may reside at each sensor location. The three types are

- range radar wherein range (r^i), azimuth (Γ^i) and elevation (θ^i) data are available,

· optical tracker wherein azimuth and elevation data are available, and

· doppler radar wherein range, range rate ($\dot{r}i$), azimuth and elevation data are available.

The observational equations in terms of the global state are

$$r^i = ((x^1-d^{i,1})^2 + (x^2-d^{i,2})^2 + (x^3-d^{i,3})^2)^{1/2} \tag{50}$$

$$\theta^i = \sin^{-1} \frac{[0\ 0\ 1]\ (T^i)^{tr} \begin{bmatrix} x^1-d^{i,1} \\ x^2-d^{i,2} \\ x^3-d^{i,3} \end{bmatrix}}{((x^1-d^{i,1})^2 + (x^2-d^{i,2})^2 + (x^3-d^{i,3})^2)^{1/2}} \tag{51}$$

$$r^i = \tan^{-1} \frac{[0\ 1\ 0]\ (T^i)^{tr} \begin{bmatrix} x^1-d^{i,1} \\ x^2-d^{i,2} \\ x^3-d^{i,3} \end{bmatrix}}{[1\ 0\ 0]\ (T^i)^{tr} \begin{bmatrix} x^1-d^{i,1} \\ x^2-d^{i,2} \\ x^3-d^{i,3} \end{bmatrix}} \tag{52}$$

$$\dot{r}^i = \frac{[\ x^4\ \ x^5\ \ x^6\ ] \begin{bmatrix} x^1-d^{i,1} \\ x^2-d^{i,2} \\ x^3-d^{i,3} \end{bmatrix}}{((x^1-d^{i,1})^2 + (x^2-d^{i,2})^2 + (x^3-d^{i,3})^2)^{1/2}} \tag{53}$$

The various measurement variables are defined by Figure 1 that follows.

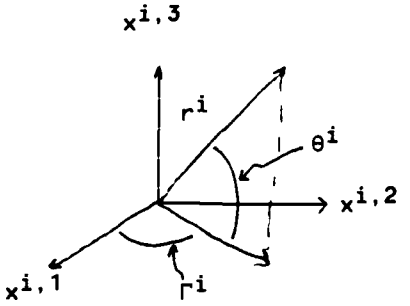

Figure 1: The Local Coordinate System and Measurement Variables

The nonlinear equations of motion (46)-(48) were integrated forwards in time starting from (30) and using the Fourth Order Runge Kutta method with a 1 second interval. Figures 2 and 3 show the resultant trajectory of the target vehicle. Comparison with the flat earth model predictions show close agreement in peak altitude (110,305. feet), terminal time (166+ seconds), and the projected path length (82.7 miles).

k	x_k^1	x_k^2	x_k^3	x_k^4	x_k^5	x_k^6
82	44,403.	226,391.	110,283.	285.5	2619.5	38.7
83	44,688.	229,010.	110,305.	285.6	2619.1	6.9
84	44,975.	231,629.	110,296.	285.8	2618.7	-24.9
.						
.						
.						
166	69,187.	444,565.	1176.	308.6	2570.3	-2640.9
167	69,496.	447,135.	-1481.	309.0	2569.6	-2673.0

Table 2: Nominal Positions and Velocities for Key Time Points of the Ballistic Trajectory

As a further check on the Fortran code for this part of the simulation, the total translational energy (kinetic plus potential) of the target vehicle was computed for each point along the computed trajectory. The total energy remained constant to within 1% as it should since there are no external forces ($u(t) = 0$) and the system is conservative. Figures 4 through 8 show some of the corresponding measurements for the various data-types with $v^i = 0$ for $\{1 \le i \le M\}$.

Each row of A(t) is computed by partial differentiating the same row of f(x(t)) w.r.t. the nominal state. Thus, A(t) has the following structure

$$A(t) = \begin{bmatrix} 0 & 0 & 0 & 1 & 0 & 0 \\ 0 & 0 & 0 & 0 & 1 & 0 \\ 0 & 0 & 0 & 0 & 0 & 1 \\ \frac{\partial x^4}{\partial x^1} & & \cdots & & & \frac{\partial x^4}{\partial x^6} \\ \vdots & & & & & \vdots \\ \frac{\partial x^6}{\partial x^1} & & \cdots & & & \frac{\partial x^6}{\partial x^6} \end{bmatrix} \qquad (54)$$

where

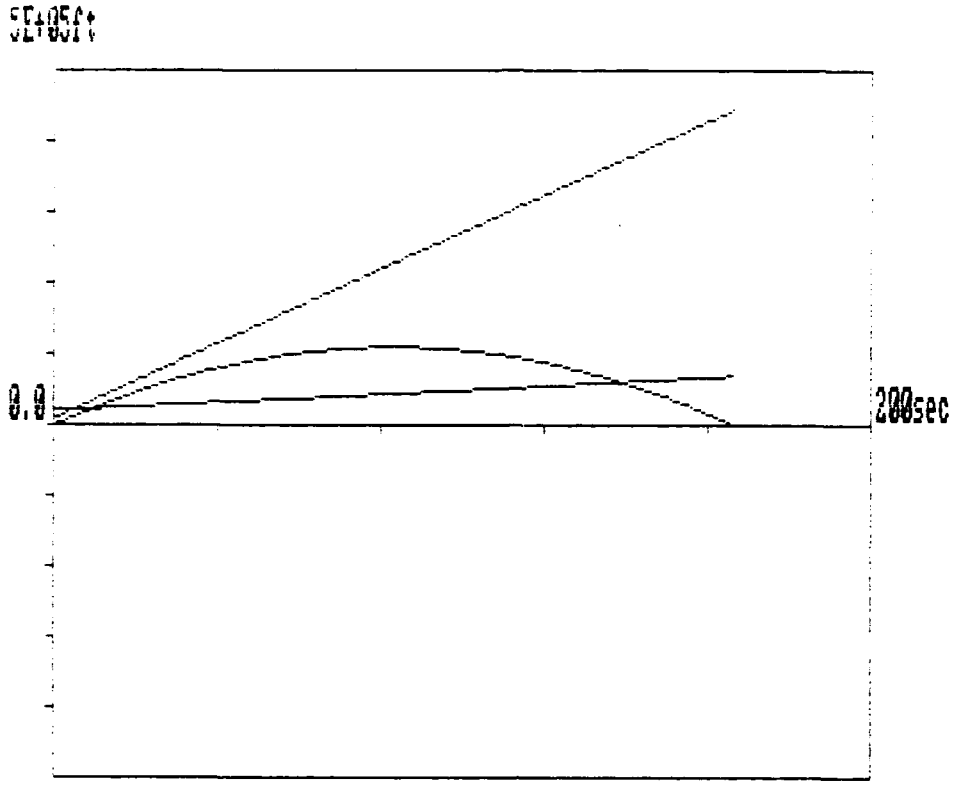

Figure 2: Nominal Position Versus Time for the Ballistic Target.

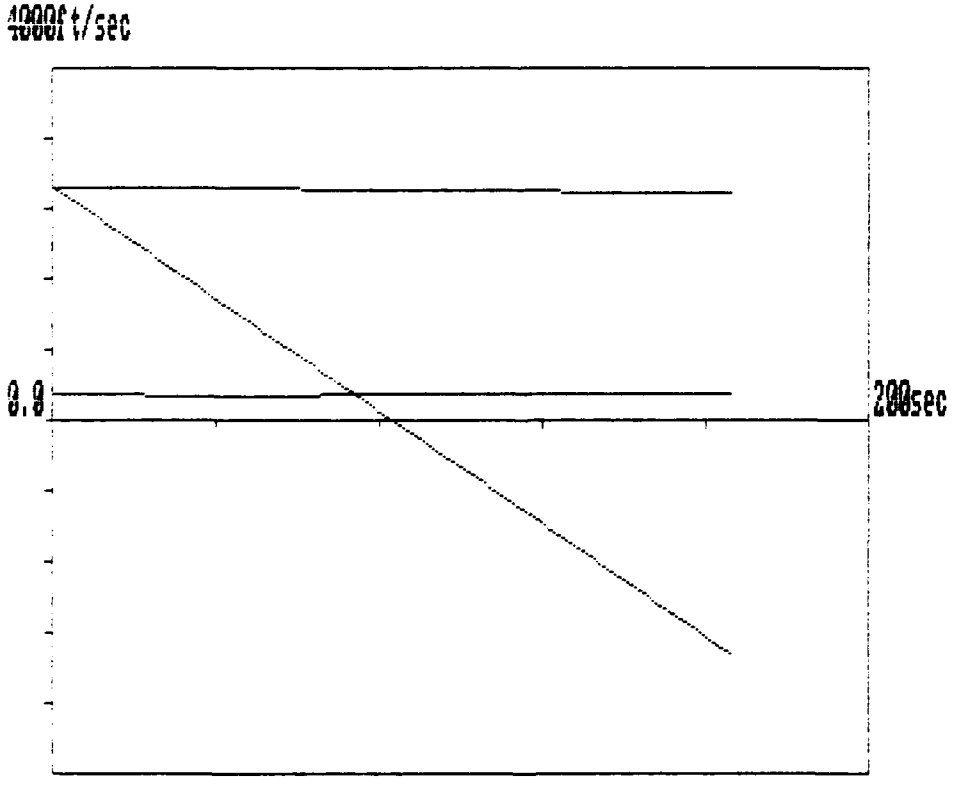

Figure 3: Nominal Velocities Versus Time for the Ballistic Target.

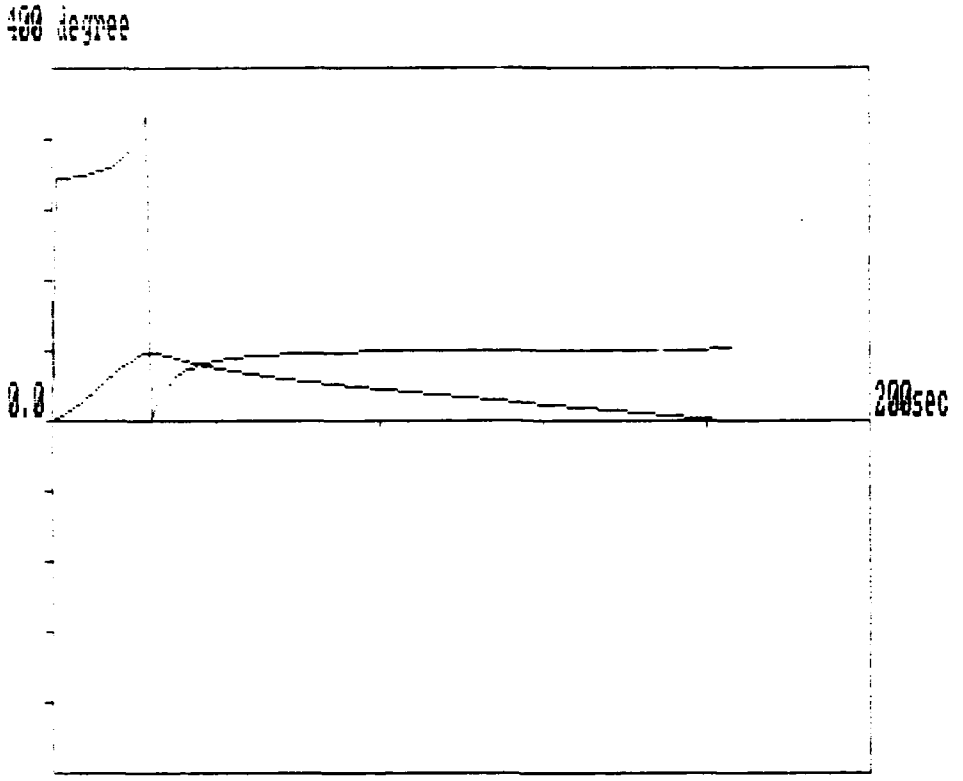

Figure 4: Sensor #1 Azimuth and Elevation Measurements Corresponding to the Nominal Ballistic Trajectory.

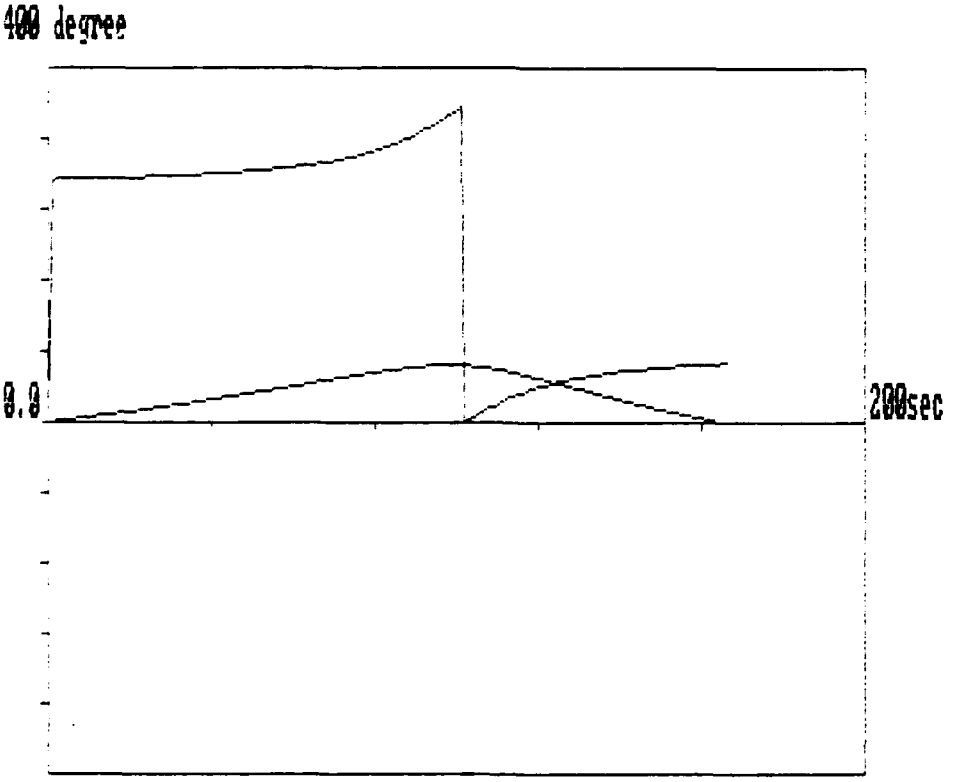

Figure 5: Sensor #2 Azimuth and Elevation Measurements Corresponding to the Nominal Ballistic Trajectory.

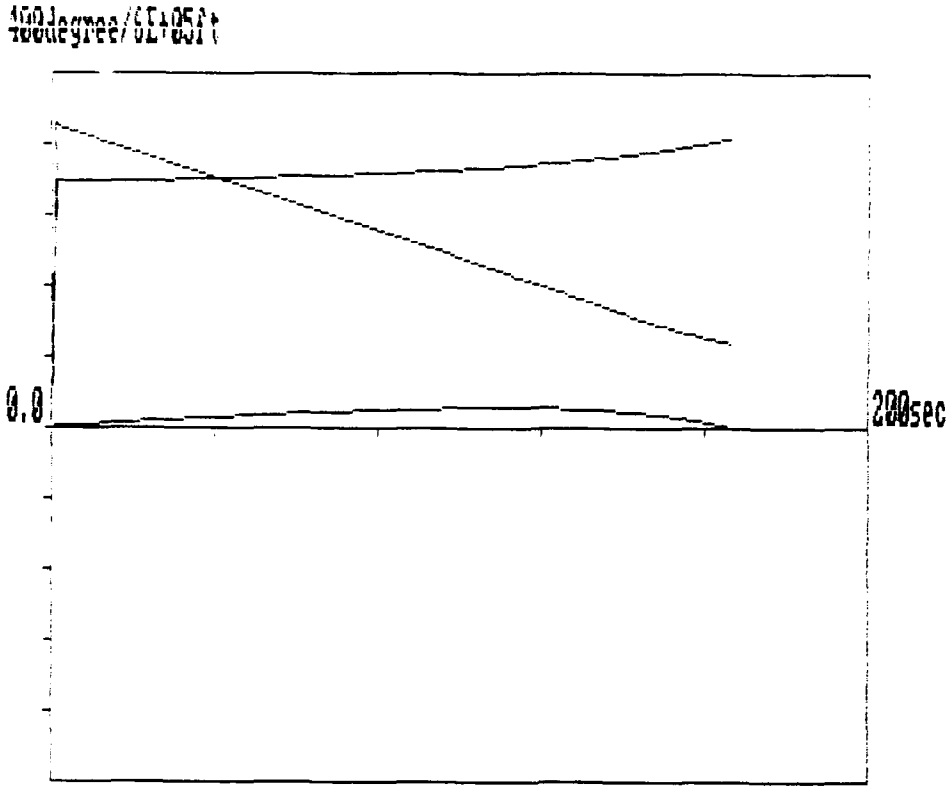

Figure 6: Sensor #3 Range, Azimuth and Elevation Measurements Corresponding to the Nominal Ballistic Trajectory.

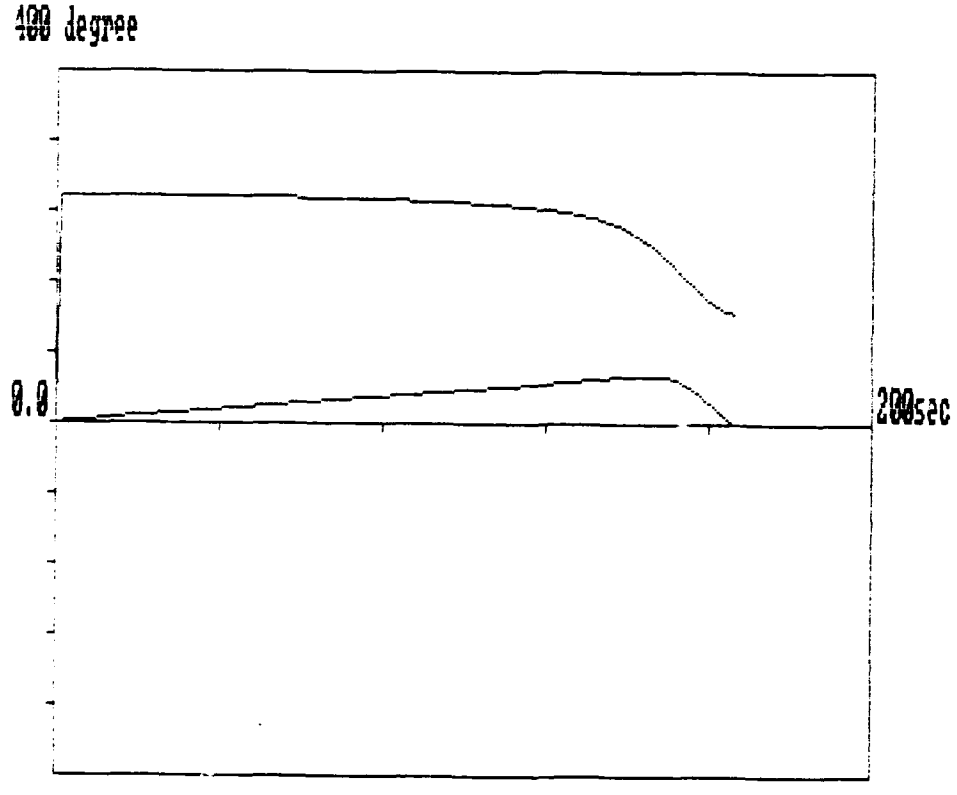

Figure 7: Sensor #4 Azimuth and Elevation Measurements Corresponding to the Nominal Ballistic Trajectory.

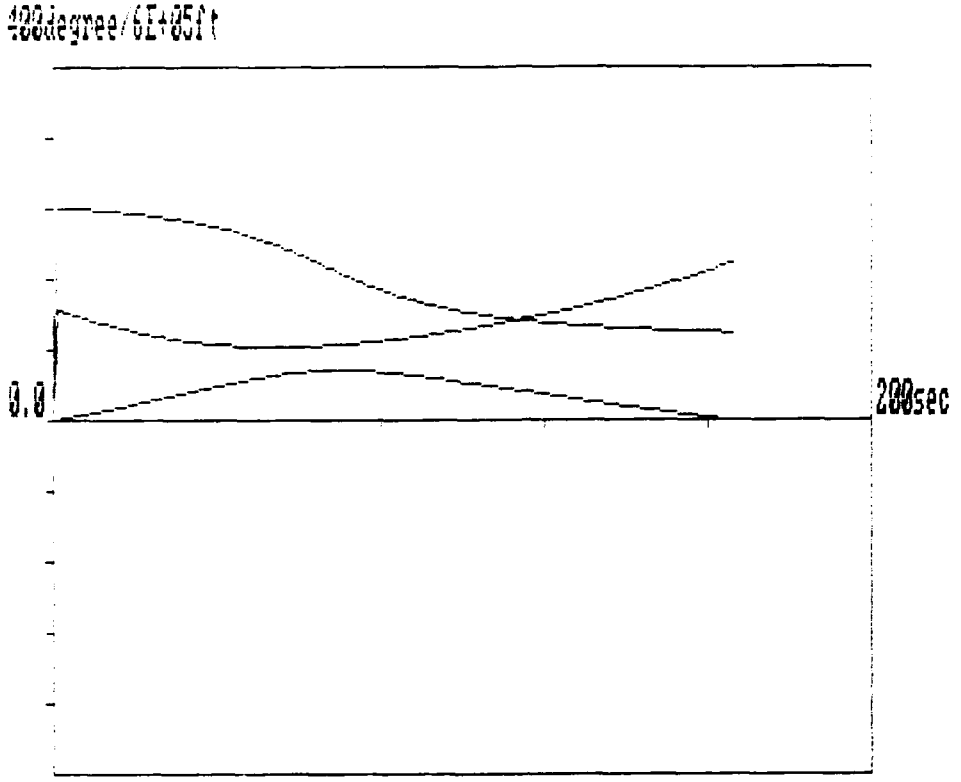

Figure 8: Sensor #5 Range, Azimuth and Elevation Measurements Corresponding to the Nominal Ballistic Trajectory.

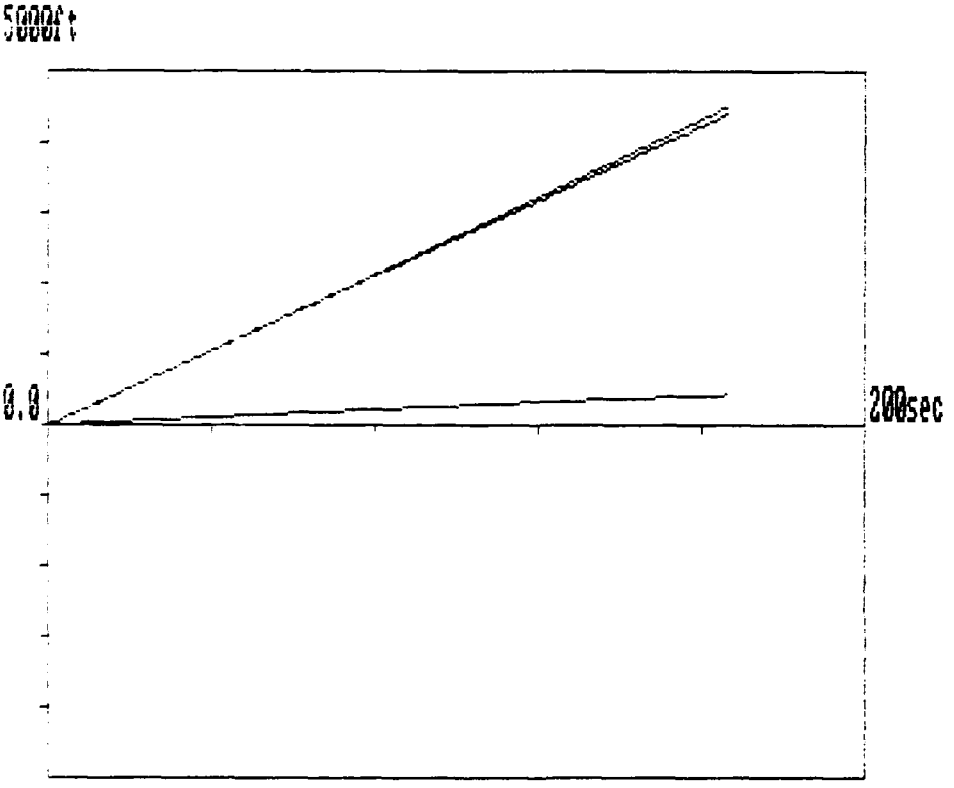

Figure 9: Perturbed State Positions Versus Time for the Ballistic Target.

$$\frac{\partial \dot{x}^4}{\partial x^1} = \frac{-\mu}{((x^1)^2 + (x^2)^2 + (x^3+r_e)^2)^{3/2}} + \frac{3\mu(x^1)^2}{((x^1)^2 + (x^2)^2 + (x^3+r_e)^2)^{5/2}} + \Omega^2 \tag{55}$$

$$\frac{\partial \dot{x}^4}{\partial x^2} = \frac{3\mu x^1 x^2}{((x^1)^2 + (x^2)^2 + (x^3+r_e)^2)^{5/2}} \tag{56}$$

$$\frac{\partial \dot{x}^4}{\partial x^3} = \frac{3\mu x^1 (x^3+r_e)}{((x^1)^2 + (x^2)^2 + (x^3+r_e)^2)^{5/2}} \tag{57}$$

$$\frac{\partial \dot{x}^4}{\partial x^4} = 0 \tag{58}$$

$$\frac{\partial \dot{x}^4}{\partial x^5} = 2\Omega \sin L \tag{59}$$

$$\frac{\partial \dot{x}^4}{\partial x^6} = -2\Omega \cos L \tag{60}$$

$$\frac{\partial \dot{x}^5}{\partial x^1} = \frac{3\mu x^1 x^2}{((x^1)^2 + (x^2)^2 + (x^3+r_e)^2)^{5/2}} \tag{61}$$

$$\frac{\partial \dot{x}^5}{\partial x^2} = \frac{-\mu}{((x^1)^2 + (x^2)^2 + (x^3+r_e)^2)^{3/2}} + \frac{3\mu(x^2)^2}{((x^1)^2 + (x^2)^2 + (x^3+r_e)^2)^{5/2}} + \Omega^2 \sin^2 L \tag{62}$$

$$\frac{\partial \dot{x}^5}{\partial x^3} = \frac{3\mu x^2 (x^3+r_e)}{((x^1)^2 + (x^2)^2 + (x^3+r_e)^2)^{5/2}} - \Omega^2 \cos L \sin L \tag{63}$$

$$\frac{\partial \dot{x}^5}{\partial x^4} = -2\Omega \sin L \tag{64}$$

$$\frac{\partial \dot{x}^5}{\partial x^5} = 0 \tag{65}$$

$$\frac{\partial \dot{x}^5}{\partial x^6} = 0 \tag{66}$$

$$\frac{\partial \dot{x}^6}{\partial x^1} = \frac{3\mu x^1 (x^3+r_e)}{((x^1)^2 + (x^2)^2 + (x^3+r_e)^2)^{5/2}} \tag{67}$$

$$\frac{\partial \dot{x}^6}{\partial x^2} = \frac{3\mu x^2 (x^3+r_e)}{((x^1)^2 + (x^2)^2 + (x^3+r_e)^2)^{5/2}} - \Omega^2 \cos L \sin L \tag{68}$$

$$\frac{\partial \dot{x}^6}{\partial x^3} = \frac{-\mu}{((x^1)^2 + (x^2)^2 + (x^3+r_e)^2)^{3/2}} + \frac{3\mu (x^3+r_e)^2}{((x^1)^2 + (x^2)^2 + (x^3+r_e)^2)^{5/2}} + \Omega^2 \cos^2 L \tag{69}$$

$$\frac{\partial \dot{x}^6}{\partial x^4} = 2\Omega \cos L \tag{70}$$

$$\frac{\partial \dot{x}^6}{\partial x^5} = 0 \tag{71}$$

$$\frac{\partial \dot{x}^6}{\partial x^6} = 0 \tag{72}$$

Each row of $C^i(t)$ is computed by partial differentiating the same row of hi(x(t) w.r.t. the nominal state. Thus, when the ith sensor is a doppler radar, $C^i(t)$ has the following structure

$$C^i(t) = \begin{bmatrix} \frac{\partial r^i}{\partial x^1} & \cdots & \frac{\partial r^i}{\partial x^3} & 0 & 0 & 0 \\ \frac{\partial \dot{r}^i}{\partial x^1} & & & & & \frac{\partial \dot{r}^i}{\partial x^6} \\ \frac{\partial r^i}{\partial x^1} & \cdots & \frac{\partial r^i}{\partial x^3} & 0 & 0 & 0 \\ \frac{\partial \theta^i}{\partial x^1} & \cdots & \frac{\partial \theta^i}{\partial x^3} & 0 & 0 & 0 \end{bmatrix} \quad (73)$$

where

$$\frac{\partial r^i}{\partial x^1} = \frac{x^1 - d^{i,1}}{((x^1-d^{i,1})^2 + (x^2-d^{i,2})^2 + (x^3-d^{i,3})^2)^{1/2}} \quad (74)$$

$$\frac{\partial r^i}{\partial x^2} = \frac{x^2 - d^{i,2}}{((x^1-d^{i,1})^2 + (x^2-d^{i,2})^2 + (x^3-d^{i,3})^2)^{1/2}} \quad (75)$$

$$\frac{\partial r^i}{\partial x^3} = \frac{x^3 - d^{i,3}}{((x^1-d^{i,1})^2 + (x^2-d^{i,2})^2 + (x^3-d^{i,3})^2)^{1/2}} \quad (76)$$

$$\frac{\partial \dot{r}^i}{\partial x^4} = \frac{\partial \dot{r}^i}{\partial x^5} = \frac{\partial \dot{r}^i}{\partial x^6} = 0 \quad (77)$$

$$\frac{\partial \dot{r}^i}{\partial x^1} = -\frac{(x^4(x^1-d^{i,1}) + x^5(x^2-d^{i,2}) + x^6(x^3-d^{i,3}))(x^1-d^{i,1})}{((x^1-d^{i,1})^2 + (x^2-d^{i,2})^2 + (x^3-d^{i,3})^2)^{3/2}} \quad (78)$$

$$+ \frac{x^4}{((x^1-d^{i,1})^2 + (x^2-d^{i,2})^2 + (x^3-d^{i,3})^2)^{1/2}} \quad (79)$$

$$\frac{\partial \dot{r}^i}{\partial x^2} = -\frac{(x^4(x^1-d^{i,1}) + x^5(x^2-d^{i,2}) + x^6(x^3-d^{i,3}))(x^2-d^{i,2})}{((x^1-d^{i,1})^2 + (x^2-d^{i,2})^2 + (x^3-d^{i,3})^2)^{3/2}}$$

$$+ \frac{x^5}{((x^1-d^{i,1})^2 + (x^2-d^{i,2})^2 + (x^3-d^{i,3})^2)^{1/2}} \tag{80}$$

$$\frac{\partial \dot{r}^i}{\partial x^3} = - \frac{(x^4(x^1-d^{i,1}) + x^5(x^2-d^{i,2}) + x^6(x^3-d^{i,3}))(x^3-d^{i,3})}{((x^1-d^{i,1})^2 + (x^2-d^{i,2})^2 + (x^3-d^{i,3})^2)^{3/2}}$$

$$+ \frac{x^6}{((x^1-d^{i,1})^2 + (x^2-d^{i,2})^2 + (x^3-d^{i,3})^2)^{1/2}} \tag{81}$$

$$\frac{\partial \dot{r}^i}{\partial x^4} = \frac{x^1-d^{i,1}}{((x^1-d^{i,1})^2 + (x^2-d^{i,2})^2 + (x^3-d^{i,3})^2)^{1/2}} \tag{82}$$

$$\frac{\partial \dot{r}^i}{\partial x^5} = \frac{x^2-d^{i,2}}{((x^1-d^{i,1})^2 + (x^2-d^{i,2})^2 + (x^3-d^{i,3})^2)^{1/2}} \tag{83}$$

$$\frac{\partial \dot{r}^i}{\partial x^6} = \frac{x^3-d^{i,3}}{((x^1-d^{i,1})^2 + (x^2-d^{i,2})^2 + (x^3-d^{i,3})^2)^{1/2}} \tag{84}$$

$$\frac{\partial \theta^i}{\partial x^1} = \frac{1}{(1-u^2)^{1/2}} - \frac{[0\ 0\ 1]\ (T^i)^{tr} \begin{bmatrix} x^1-d^{i,1} \\ x^2-d^{i,2} \\ x^3-d^{i,3} \end{bmatrix} (x^1-d^{i,1})}{((x^1-d^{i,1})^2 + (x^2-d^{i,2})^2 + (x^3-d^{i,3})^2)^{3/2}}$$

$$+ \frac{[0\ 0\ 1]\ (T^i)^{tr} \begin{bmatrix} 1 \\ 0 \\ 0 \end{bmatrix}}{((x^1-d^{i,1})^2 + (x^2-d^{i,2})^2 + (x^3-d^{i,3})^2)^{1/2}} \tag{85}$$

where u is the argument of $\sin^{-1}$ in equation (51).

$$\frac{\partial \theta^i}{\partial x^2} = \frac{1}{(1-u^2)^{1/2}} \left[- \frac{[0\ 0\ 1]\ (T^i)^{tr} \begin{bmatrix} x^1-d^{i,1} \\ x^2-d^{i,2} \\ x^3-d^{i,3} \end{bmatrix} (x^2-d^{i,2})}{((x^1-d^{i,1})^2 + (x^2-d^{i,2})^2 + (x^3-d^{i,3})^2)^{3/2}} + \frac{[0\ 0\ 1]\ (T^i)^{tr} \begin{bmatrix} 0 \\ 1 \\ 0 \end{bmatrix}}{((x^1-d^{i,1})^2 + (x^2-d^{i,2})^2 + (x^3-d^{i,3})^2)^{1/2}} \right] \tag{86}$$

$$\frac{\partial \theta^i}{\partial x^3} = \frac{1}{(1-u^2)^{1/2}} \left[- \frac{[0\ 0\ 1]\ (T^i)^{tr} \begin{bmatrix} x^1-d^{i,1} \\ x^2-d^{i,2} \\ x^3-d^{i,3} \end{bmatrix} (x^3-d^{i,3})}{((x^1-d^{i,1})^2 + (x^2-d^{i,2})^2 + (x^3-d^{i,3})^2)^{3/2}} + \frac{[0\ 0\ 1]\ (T^i)^{tr} \begin{bmatrix} 0 \\ 0 \\ 1 \end{bmatrix}}{((x^1-d^{i,1})^2 + (x^2-d^{i,2})^2 + (x^3-d^{i,3})^2)^{1/2}} \right] \tag{87}$$

$$\frac{\partial \theta^i}{\partial x^4} = \frac{\partial \theta^i}{\partial x^5} = \frac{\partial \theta^i}{\partial x^6} = 0 \tag{88}$$

$$\frac{\partial r^i}{\partial x^1} = \frac{1}{(1+u^2)} \left[- \frac{[0\ 1\ 0]\ (T^i)^{tr} \begin{bmatrix} x^1-d^{i,1} \\ x^2-d^{i,2} \\ x^3-d^{i,3} \end{bmatrix} [1\ 0\ 0]\ (T^i)^{tr} \begin{bmatrix} 1 \\ 0 \\ 0 \end{bmatrix}}{\left([1\ 0\ 0]\ (T^i)^{tr} \begin{bmatrix} x^1-d^{i,1} \\ x^2-d^{i,2} \\ x^3-d^{i,3} \end{bmatrix} \right)^2} \right]$$

$$+ \frac{[0\ 1\ 0]\ (T^i)^{tr} \begin{bmatrix} 1 \\ 0 \\ 0 \end{bmatrix}}{[1\ 0\ 0]\ (T^i)^{tr} \begin{bmatrix} x^1-d^{i,1} \\ x^2-d^{i,2} \\ x^3-d^{i,3} \end{bmatrix}} \tag{89}$$

where u is now the argument of $\tan^{-1}$ in equation (52).

$$\frac{\partial r^i}{\partial x^2} = \frac{1}{(1+u^2)} \left[- \frac{[0\ 1\ 0]\ (T^i)^{tr} \begin{bmatrix} x^1-d^{i,1} \\ x^2-d^{i,2} \\ x^3-d^{i,3} \end{bmatrix} [1\ 0\ 0]\ (T^i)^{tr} \begin{bmatrix} 0 \\ 1 \\ 0 \end{bmatrix}}{\left([1\ 0\ 0]\ (T^i)^{tr} \begin{bmatrix} x^1-d^{i,1} \\ x^2-d^{i,2} \\ x^3-d^{i,3} \end{bmatrix} \right)^2} \right.$$

$$\left. + \frac{[0\ 1\ 0]\ (T^i)^{tr} \begin{bmatrix} 0 \\ 1 \\ 0 \end{bmatrix}}{[1\ 0\ 0]\ (T^i)^{tr} \begin{bmatrix} x^1-d^{i,1} \\ x^2-d^{i,2} \\ x^3-d^{i,3} \end{bmatrix}} \right] \tag{90}$$

$$\frac{\partial r^i}{\partial x^3} = \frac{1}{(1+u^2)} \left[- \frac{[0\ 1\ 0]\ (T^i)^{tr} \begin{bmatrix} x^1-d^{i,1} \\ x^2-d^{i,2} \\ x^3-d^{i,3} \end{bmatrix} [1\ 0\ 0]\ (T^i)^{tr} \begin{bmatrix} 0 \\ 0 \\ 1 \end{bmatrix}}{\left([1\ 0\ 0]\ (T^i)^{tr} \begin{bmatrix} x^1-d^{i,1} \\ x^2-d^{i,2} \\ x^3-d^{i,3} \end{bmatrix} \right)^2} \right.$$

$$+ \frac{[0\ 1\ 0]\ (T^i)^{tr} \begin{bmatrix} 0 \\ 0 \\ 1 \end{bmatrix}}{[1\ 0\ 0]\ (T^i)^{tr} \begin{bmatrix} x^1 - d^{i,1} \\ x^2 - d^{i,2} \\ x^3 - d^{i,3} \end{bmatrix}} \tag{91}$$

$$\frac{\partial r^i}{\partial x^4} = \frac{\partial r^i}{\partial x^5} = \frac{\partial r^i}{\partial x^6} = 0 \tag{92}$$

The 6 biases $\alpha^i, \beta^i, \tau^i, d^{i,1}, d^{i,2}, d^{i,3}$ per local system could be included as states in the filter and estimated in order to correct for any preflight miscalibration. Then, $\alpha^i = 0$, $\beta^i = 0$ ... would be added to the equations of motion and additional partial derivative expressions would be needed. However, only the 6 positions and velocities of the target vehicle were included.

In order to create simulated data and test the state estimation part of the code, a subroutine RANDOM for generating sequences of Gaussian random vectors with prescribed covariance was written. Two algorithms were considered. The first proceeds by rotating coordinates to a system in which the covariance matrix is diagonal. In this system the multivariate normal density becomes equal to the product of its marginal densities, and each marginal density can be sampled independently of the other components. After obtaining a sample vector in this rotated system, the coordinates are rotated back to the original system.

The second algorithm proceeds by decomposing the multivariate normal density into the product of the marginal density of the first variate times the joint density of the remaining variates, conditional upon the value sampled for the first. This joint density is determined once the first variate has been sampled from its marginal density. The procedure is then applied to the second variate and iterated until values have been assigned to all components of the sample vector. This "Conditional Decomposition Algorithm" will execute more rapidly than the latter "Matrix Diagonalization Algorithm" especially for time varying covariance matrices. Thus it was chosen as the basis for subroutine RANDOM.

Assuming a constant covariance matrix, RANDOM was tested by counting the number of random values within several bands for each component. Comparison with theory has shown agreement to within a few percent. Much time was spent in validating RANDOM since its accuracy is a prerequisite for meaningful future comparisons of DSRIF estimates with decoupled Kalman filter estimates in Phase II research.

Figures 9 and 10 show the evolution of the perturbed state as governed by equation (3). The initial condition is

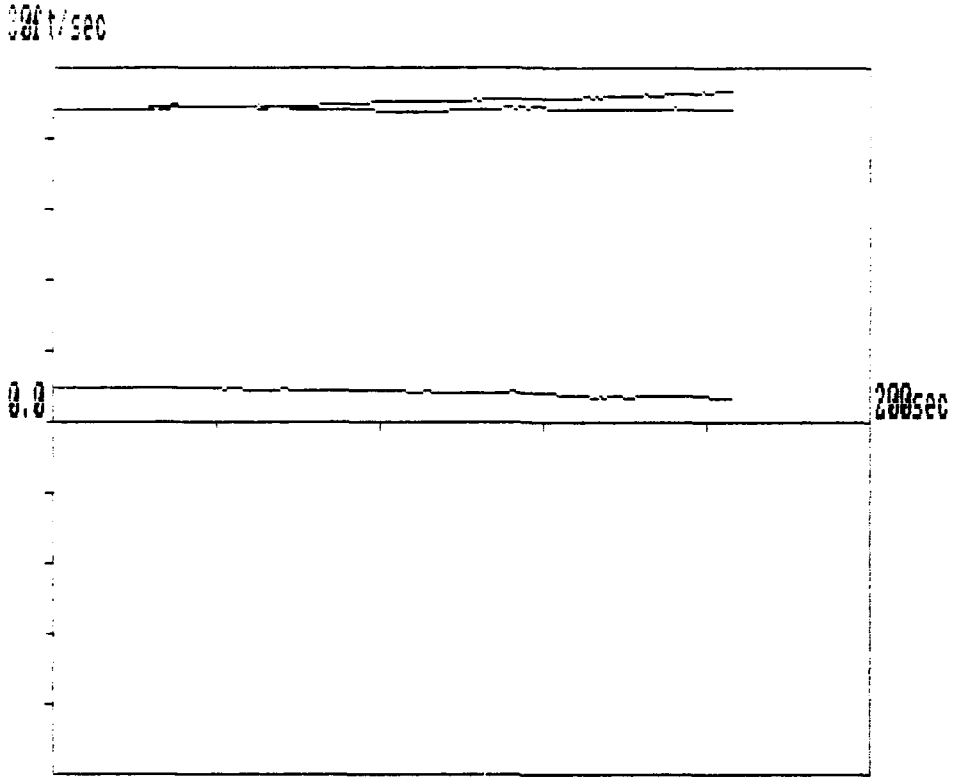

Figure 10: Perturbed State Velocities Versus Time for the Ballistic Target.

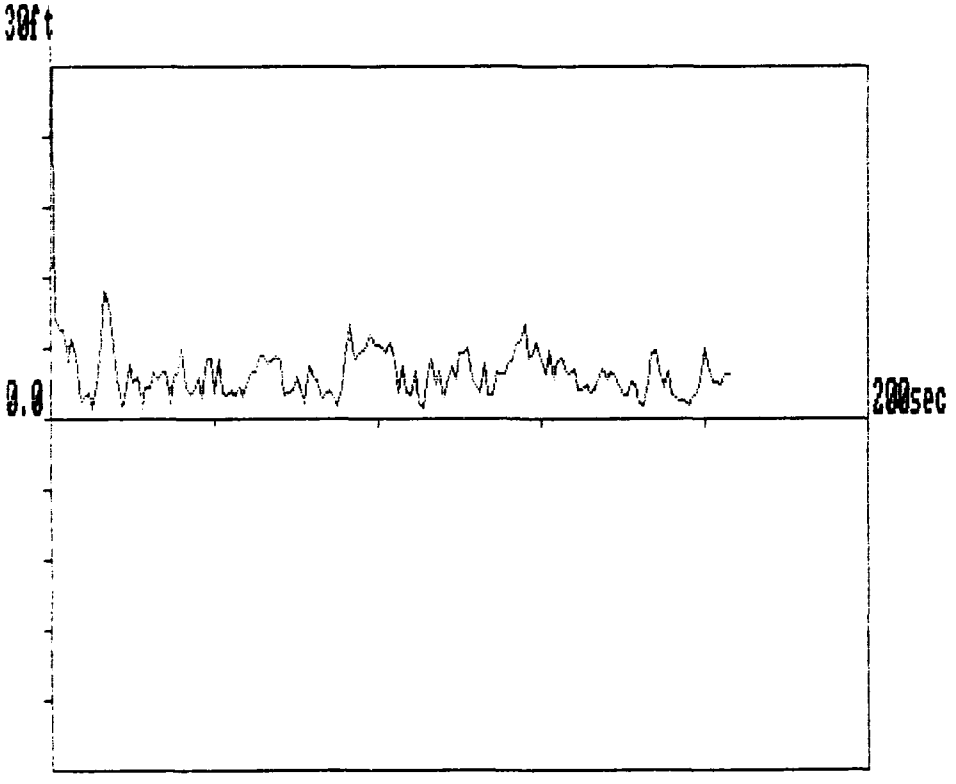

Figure 11: RMS Global Position Estimate Error Versus Time.

$$\delta x_0 = [\ 0.ft \quad 0.ft \quad 0.ft \quad 2.8629\ ft/s \quad 26.4021\ ft/s \quad 26.558\ ft/s\ ]^{tr}$$

which represents a scaling of the initial velocity vector for the nominal trajectory. Thus, the combined nominal plus perturbed solution should reach impact along the nominal line of sight (which is the vector difference between the nominal impact point and the nominal initial condition) but further from x_0 since a positive scaling factor was used. A diagonal Q_k with small variances was used to generate the process noise sequence. The position variances were .1 ft^2 and the velocity variances were .1 $(ft/s)^2$.

Figures 11, 12 and 13 are the corresponding DSRIF results with all of the prior and process noise information embedded in the merge processor. Each of the 12 local filters processed 1 measurement variable. A diagonal R_k, with variances of 10^{-5} deg^2 and 10^2 ft^2 for angular variables and range variables respectively, was used to generate the measurement noise sequence. The initial state estimate for all of the local filters was

$$\delta x_0^i = [20.ft \quad 20.ft \quad 20.ft \quad 23.8629\ ft/s \quad 47.4021\ ft/s \quad 47.558\ ft/s\ ]^{tr}$$

and a diagonal $P_0(+)$, with variances of 100 ft^2 and 100 $(ft/s)^2$ for position variables and velocity variables respectively, was used to initialize the merge processor. Figures 11 and 12 show that the rms position and velocity estimate errors quickly decay to steady state mean values after less than 10 time samples. The corresponding estimate error covariances follow the same course as expected.

In Figure 14 the process noise levels were multiplied by 10 and comparison with Figure 13 shows that the corresponding estimate error covariances increase as well. This is as expected since Q_k is linearly related to the time updated estimate error covariance i.e., the conventional covariance time update equation is given by

$$P_{k+1}(-) = \Phi_k P_k(+) \Phi_k^{tr} + Q_k \tag{93}$$

Furthermore, the same phenomenon results when R_k is multiplied by a factor of 5 in Figure 15. The conventional covariance measurement update equation in Josephson Stabilized form

$$P_k(+) = [I - K_k H_k]\ P_k(-)\ [I - K_k H_k]^{tr} + K_k R_k K_k^{tr} \tag{94}$$

may be combined with the Kalman gain equation

$$K_k = P_k(-) H_k^{tr}\ [H_k P_k(-) H_k^{tr} + R_k]^{-1} \tag{95}$$

to show that the time updated estimate error covariance is linearly related to R_k as well. The result is that

$$P_k^{-1}(+) = P_k^{-1}(-) + H_k^{tr}\ R_k^{-1}\ H_k \tag{96}$$

2.3 Extended-Decentralized Square Root Information Filtering of MLRS Data

On November 11, 1987 six rockets were launched sequentially in time over a period of 2 hours and 30 minutes at WSMR. Only 1 rocket was airborne at any

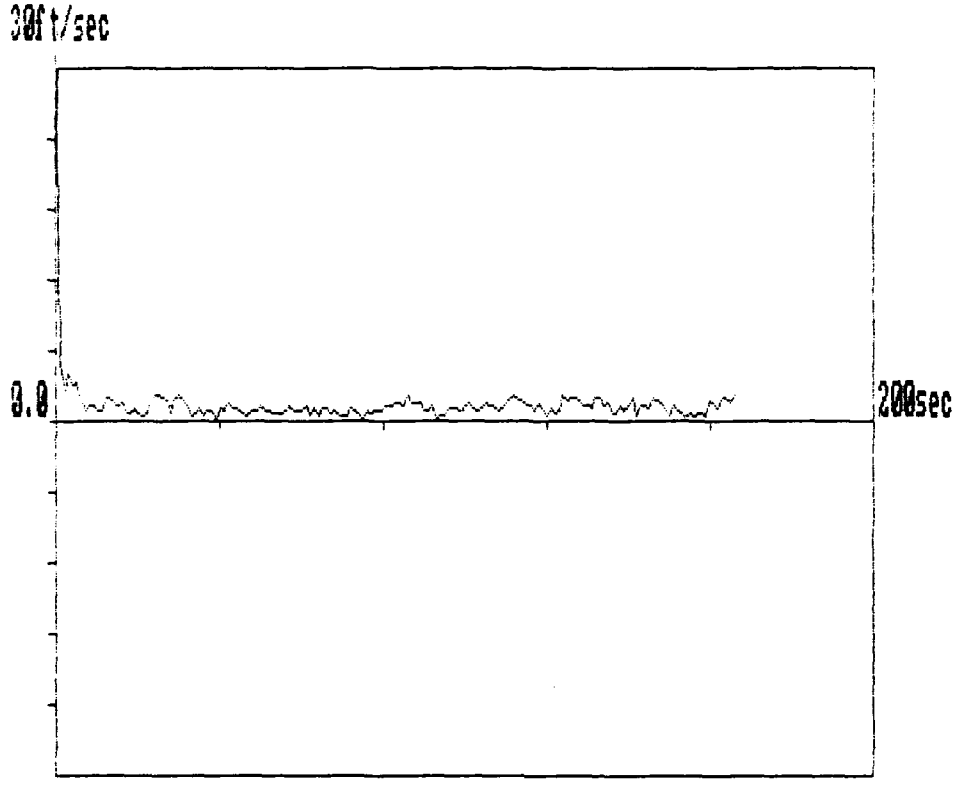

Figure 12: RMS Global Velocity Estimate Error Versus Time.

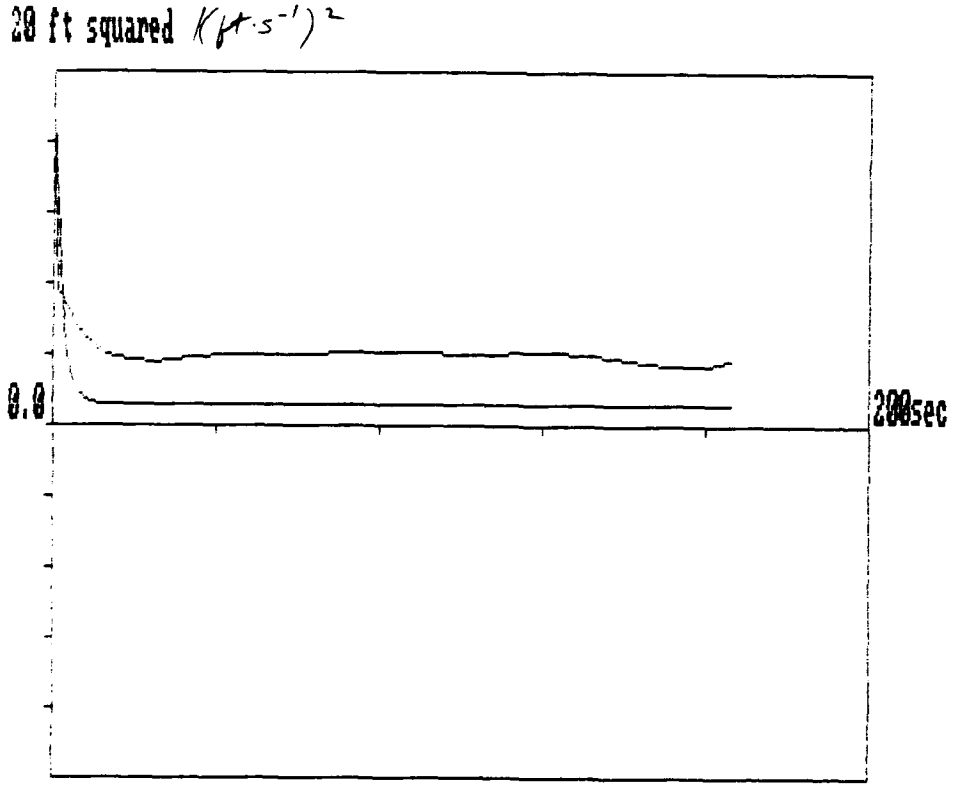

Figure 13: Global Position and Velocity Estimate Error Covariances Versus Time. $R_k(j,j)=10^{-5}$ for angle variables and 10^2 for range variables. $Q_k(j,j) = .1$ for all $j=1,\ldots,6$.

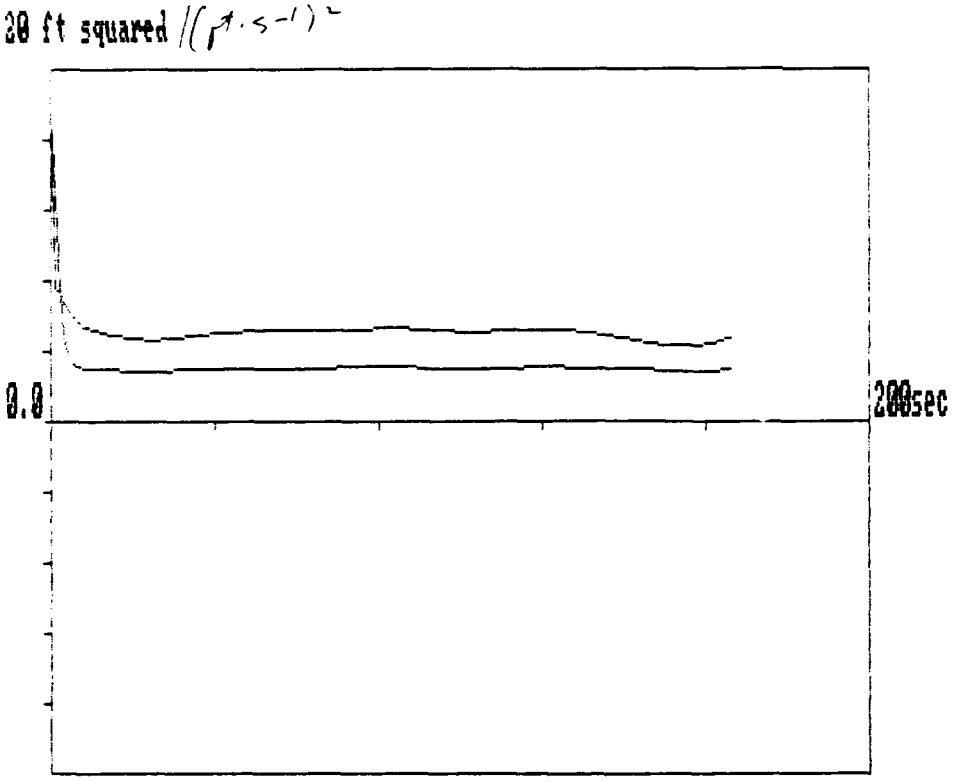

Figure 14: Global Position and Velocity Estimate Error Covariances Versus Time. $R_k(j,j)=10^{-5}$ for angle variables and 10^2 for range variables. $Q_k(j,j) = 1.$ for all $j=1,\ldots,6$.

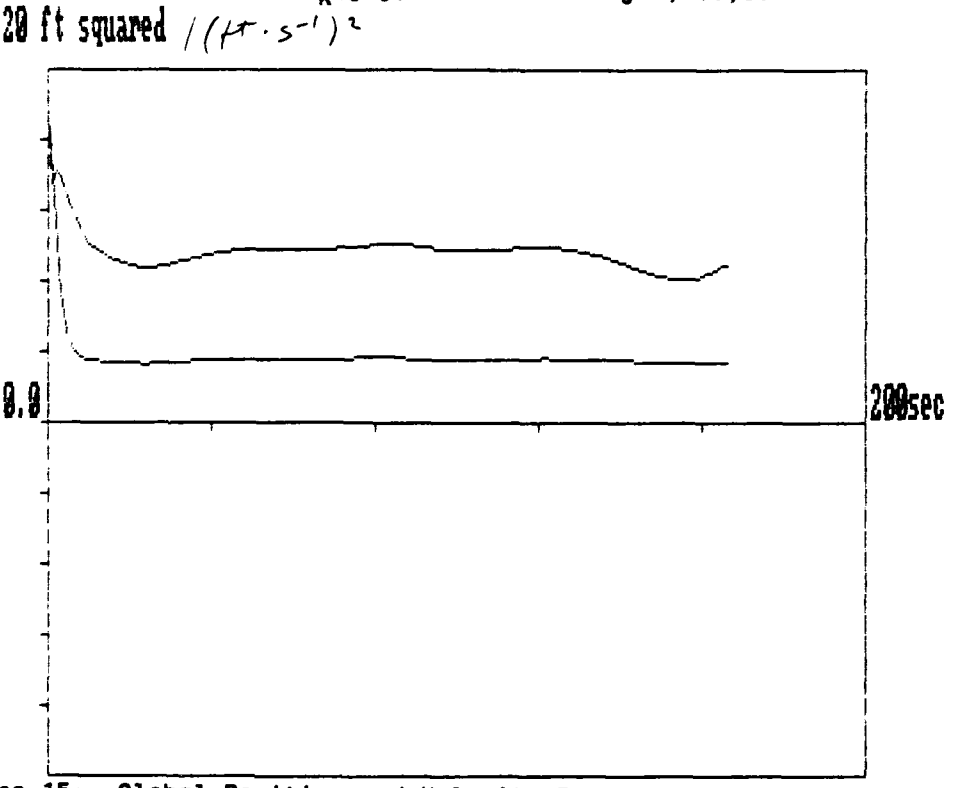

Figure 15: Global Position and Velocity Estimate Error Covariances Versus Time. $R_k(j,j)=5 \times 10^{-5}$ for angle variables and 5×10^2 for range variables. $Q_k(j,j) = 1.$ for all $j=1,\ldots,6$.

one time and thus data association for multitarget tracking would not be needed. MTI obtained a copy of the Multiple Launch Rocket System (MLRS) data in order to gain experience at processing real test range single target data with the algorithm. The digitized measurements for all six shots were plotted in order to select the best set as characterized by the least amount of data drop outs and outlyers. Figures 16 through 26 comprise the data set chosen and this was the second shot.

The MLRS data set contained azimuth and elevation angle measurements (with respect to each local sensor) from 11 optical trackers located at the range coordinates listed in Table 3 below. The origin of the WSCS is [500,000. 500,000. 0.] in units of feet with its latitude and longitude equal to 32.38 and 106.481 degrees respectively. Each optical tracker is also characterized by a set of 3 Euler angles α^i, β^i and τ^i which define its orientation relative to the Global Coordinate System (GCS) as in section 2.2. The first two angles are calculated using equations (39) through (45) and the angular misalignment is assumed equal to 0.

i	Optical Tracker	$d^{i,1}$	$d^{i,2}$	$d^{i,3}$	α^i	β^i	τ^i
1	G110	7,308.2856	-237,899.4738	2,686.4839	32.4320	106.3096	0.
2	G152	3,440.0051	-225,071.0857	2,810.1186	32.4671	106.3221	0.
3	G 30	-32,914.1744	-203,310.5045	3,352.4878	32.5267	106.4402	0.
4	G 80	-25,713.6722	-221,819.8655	2,778.9435	32.4760	106.4167	0.
5	G102	-26,675.1965	-244.187.0879	2,523.8507	32.4148	106.4198	0.
6	G106	-19,918.2179	-252,889.6291	2,452.5578	32.3910	106.3979	0.
7	G150	- 6,758.5768	-201,753.4857	2,992.5174	32.5310	106.3552	0.
8	G220	-32,505.5910	-181,663.7427	3,539.5030	32.5859	106.4389	0.
9	G252	3,844.5713	-168,382.0272	3,299.8877	32.6223	106.3208	0.
10	G254	2,449.5559	-152,952.6079	3,436.9316	32.6646	106.3253	0.
11	G256	-38,799.7405	-157,557.3009	3,506.5874	32.6519	106.4595	0.

Table 3: Optical Tracker Locations and Orientations in GCS for the MLRS Test

The data set also contained range, azimuth and elevation angle measurements from 3 radars but with respect to the local coordinate system originating at the launcher. Their locations and orientations are given in Table 4 below however, the launcher location $d^{i,1}$ = -14,074.34, $d^{i,2}$ = -247,569.51, $d^{i,3}$ = 2,505.08 was used instead.

i	Radar	$d^{i,1}$	$d^{i,2}$	$d^{i,3}$	α^i	β^i	τ^i
12	350	-13,971.87	-264,430.55	2,334.06	32.3594	106.3786	0.
13	393	-27,098.86	-222,179.08	2,787.84	32.4750	106.4212	0.
14	394	- 2,382.95	-260,481.11	2,403.07	32.3702	106.3410	0.

Table 4: Radar Locations and Orientations in GCS for the MLRS Test

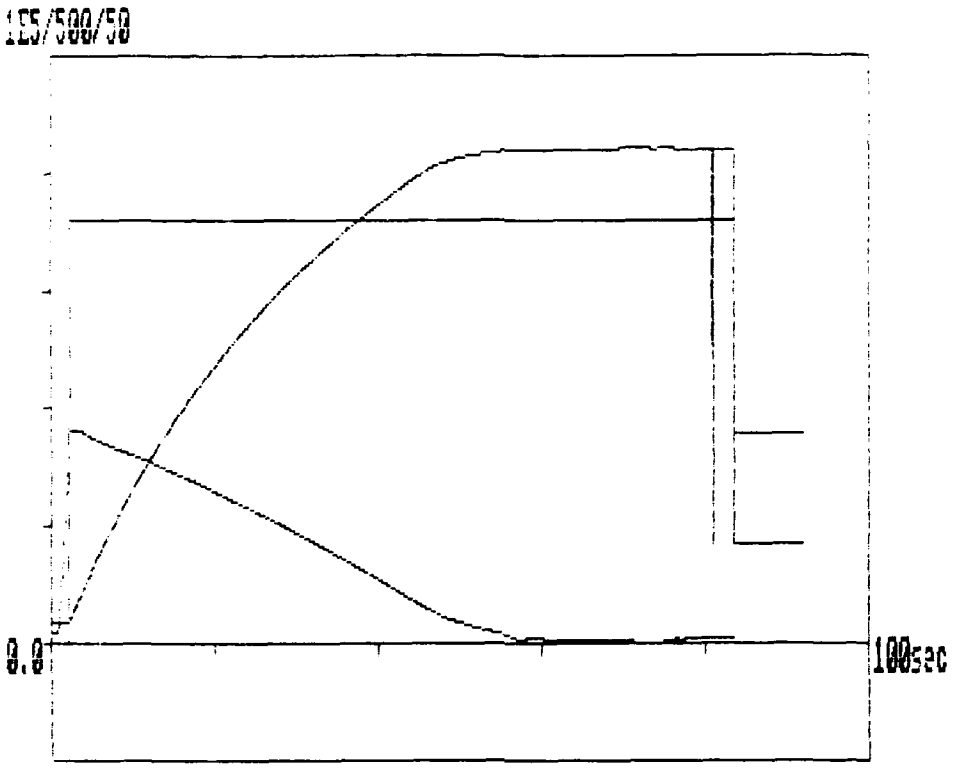

Figure 16: Radar #350 Range, Azimuth and Elevation Measurements for MRLS.

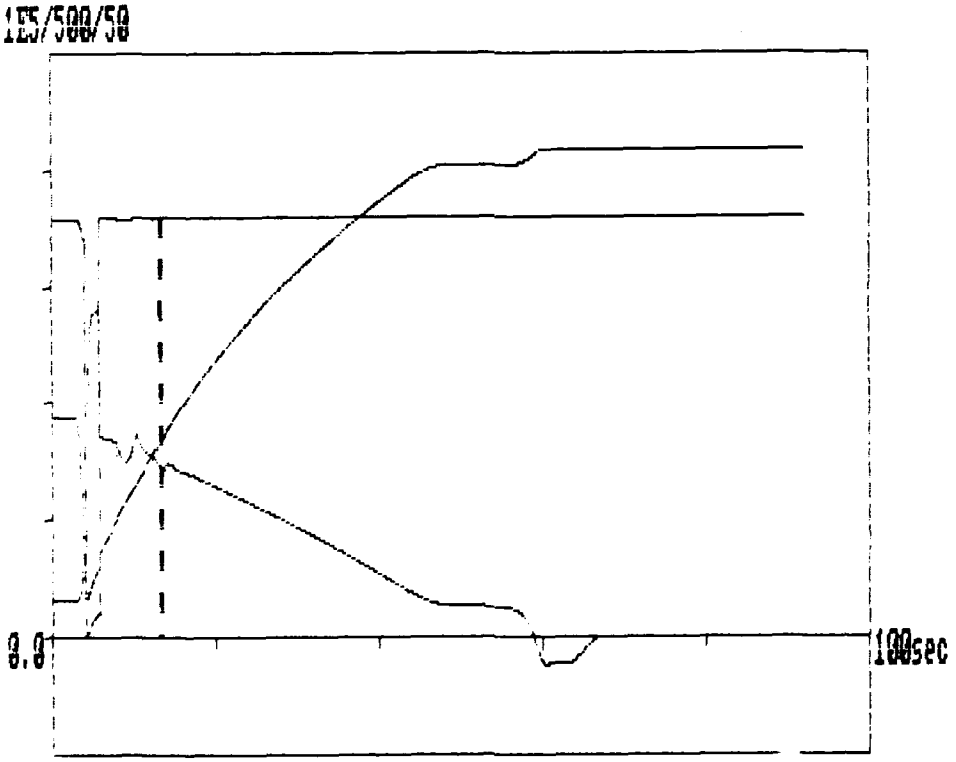

Figure 17: Radar #393 Range, Azimuth and Elevation Measurements for MRLS.

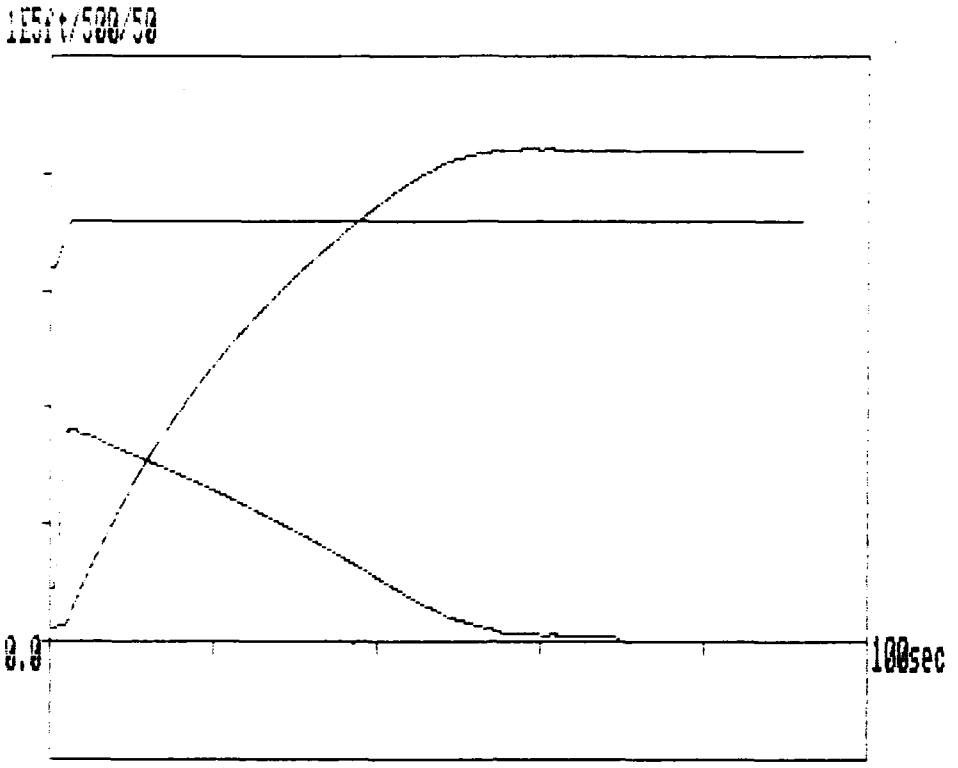

Figure 18: Radar #394 Range, Azimuth and Elevation Measurements for MRLS.

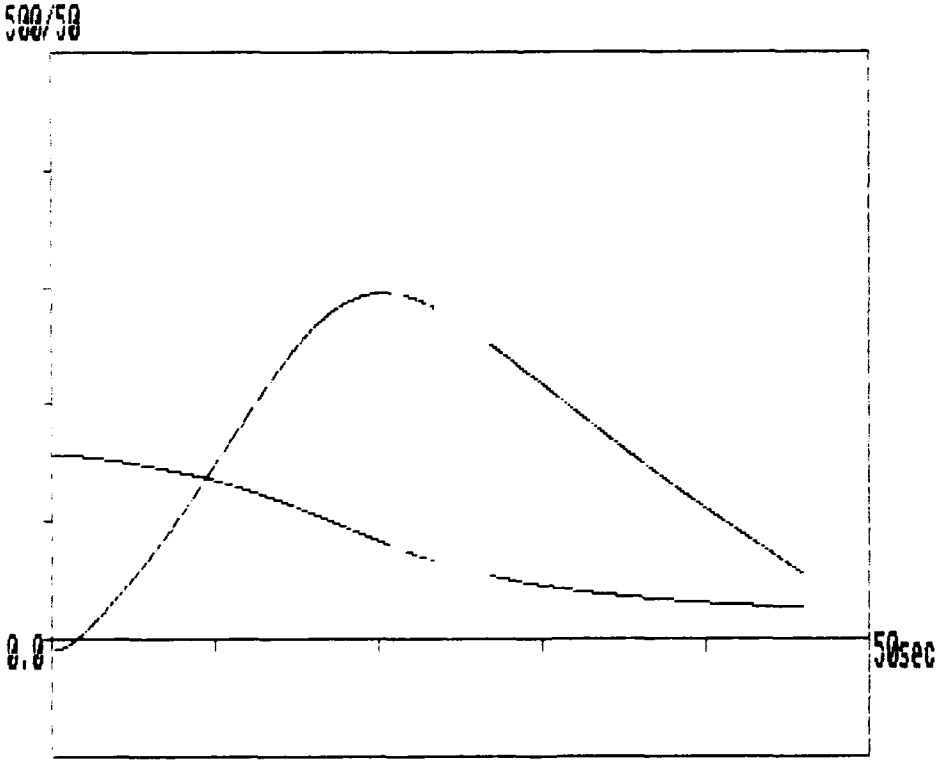

Figure 19: G30 Azimuth and Elevation Measurements for MRLS.

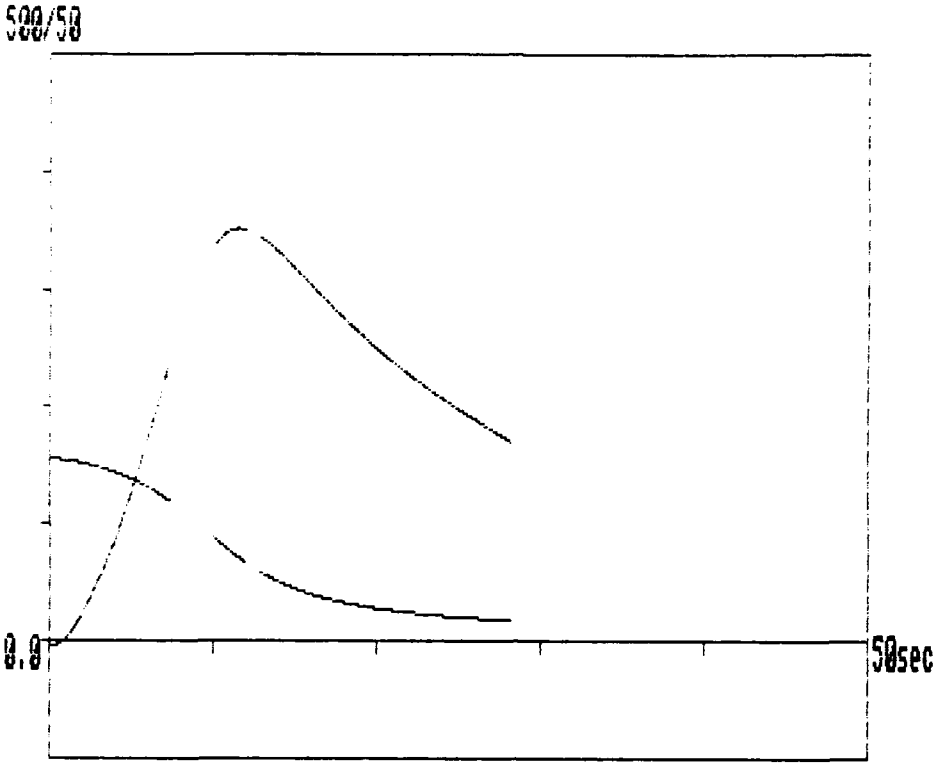

Figure 20: G80 Azimuth and Elevation Measurements for MRLS.

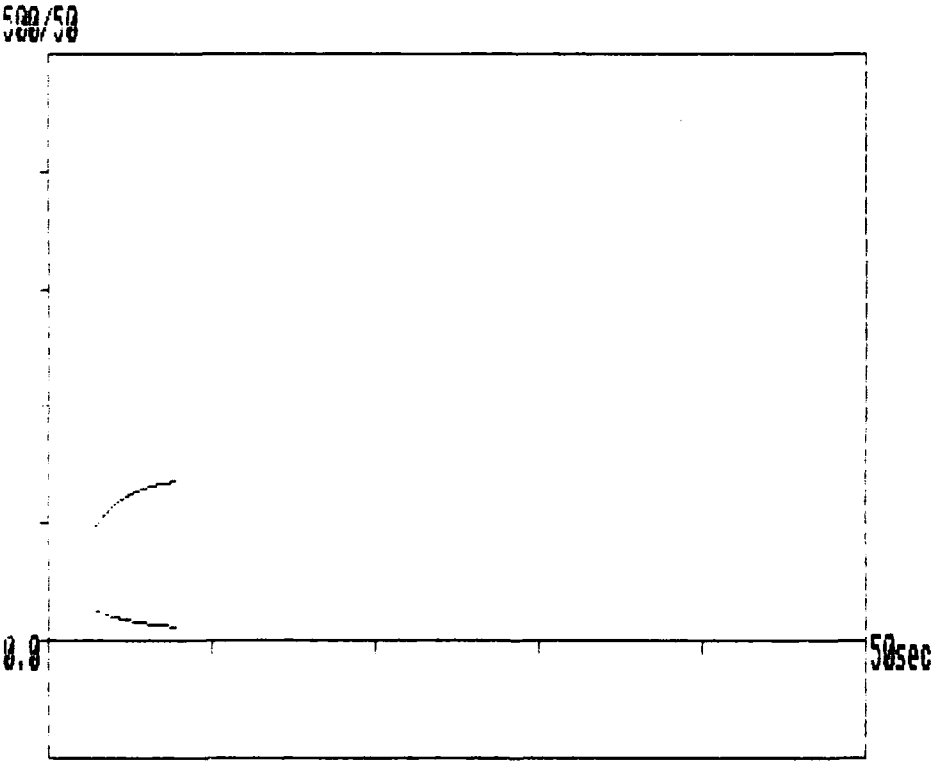

Figure 21: G106 Azimuth and Elevation Measurements for MRLS.

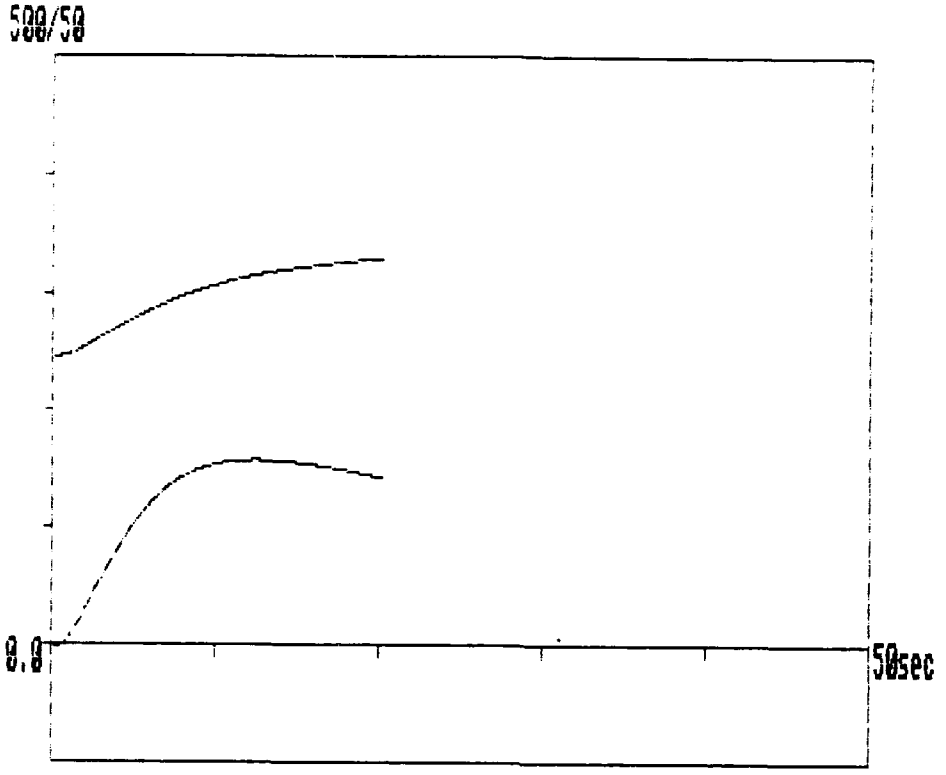

Figure 22: G110 Azimuth and Elevation Measurements for MRLS.

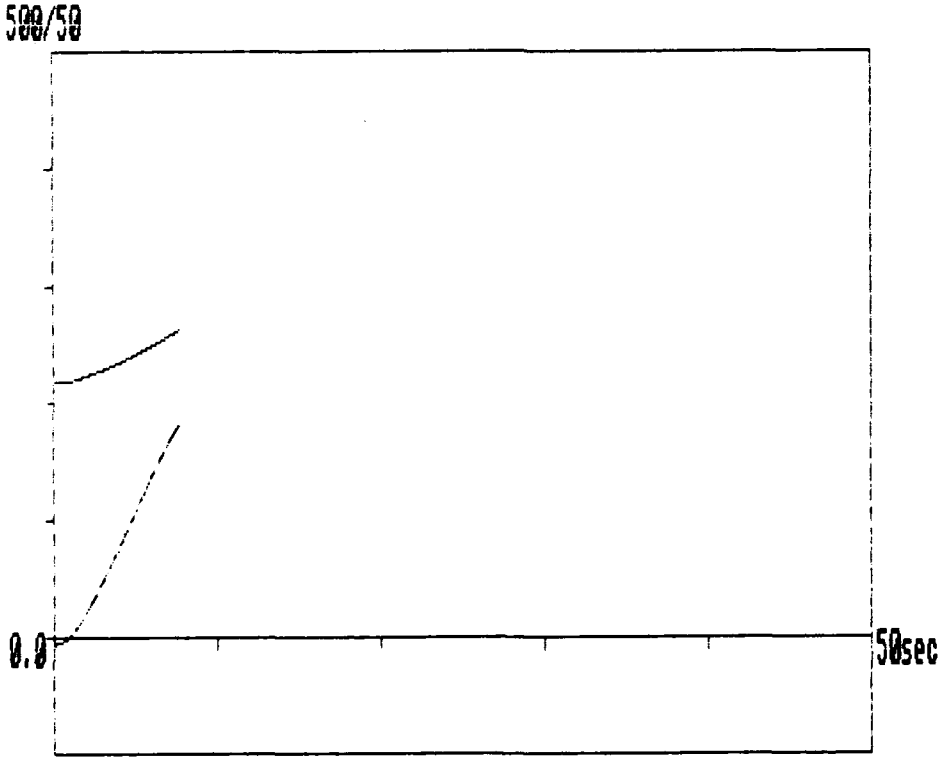

Figure 23: G152 Azimuth and Elevation Measurements for MRLS.

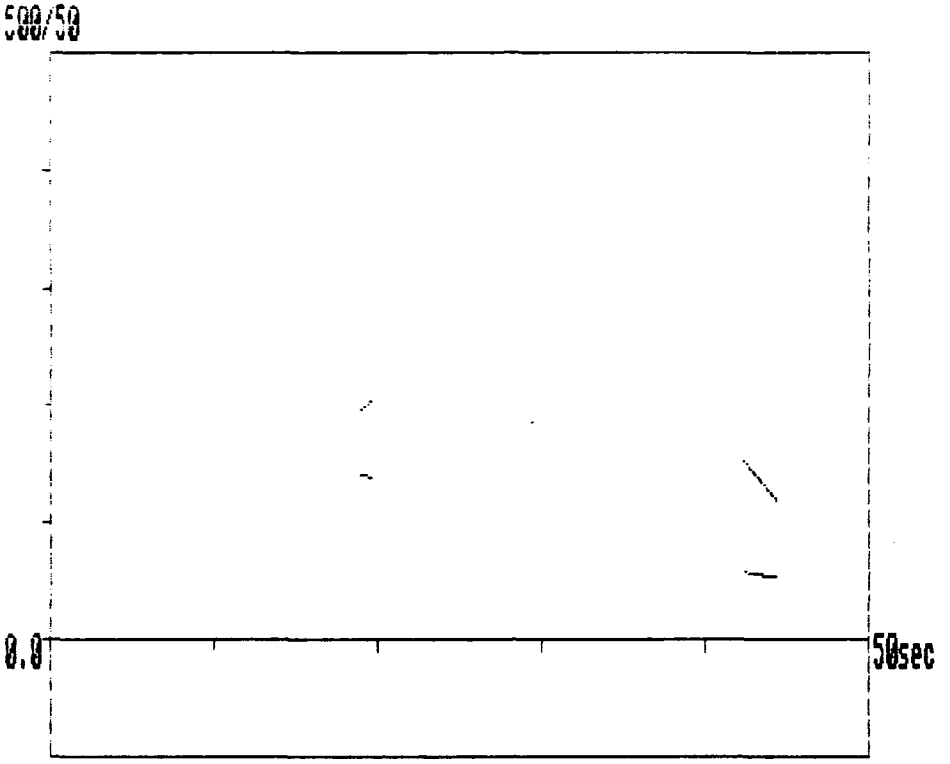

Figure 24: G220 Azimuth and Elevation Measurements for MRLS.

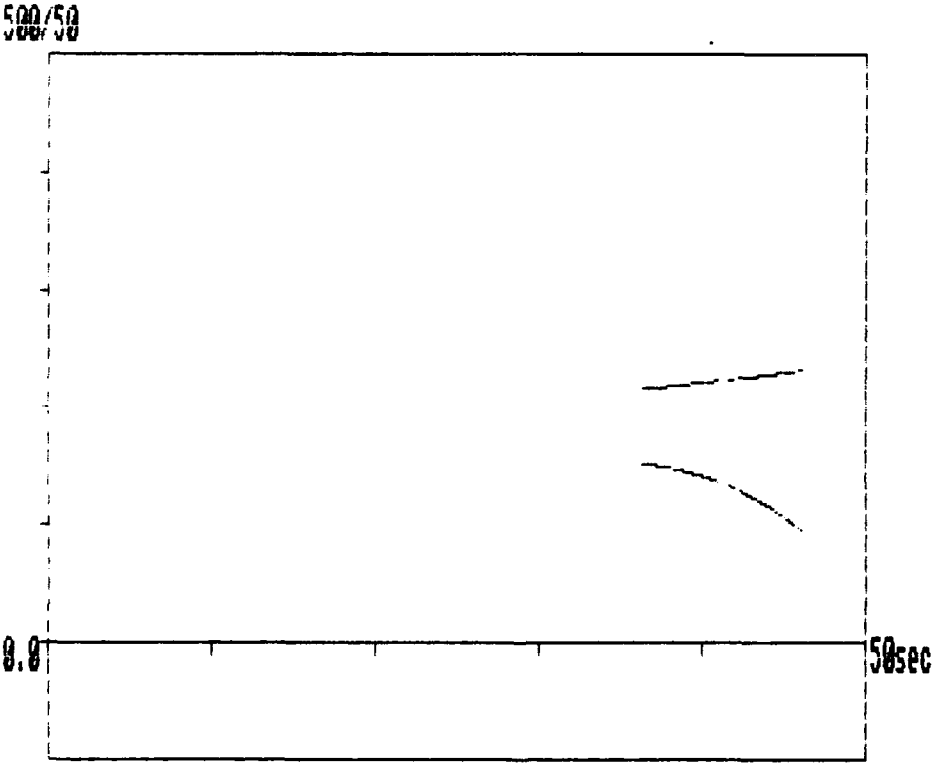

Figure 25: G254 Azimuth and Elevation Measurements for MRLS.

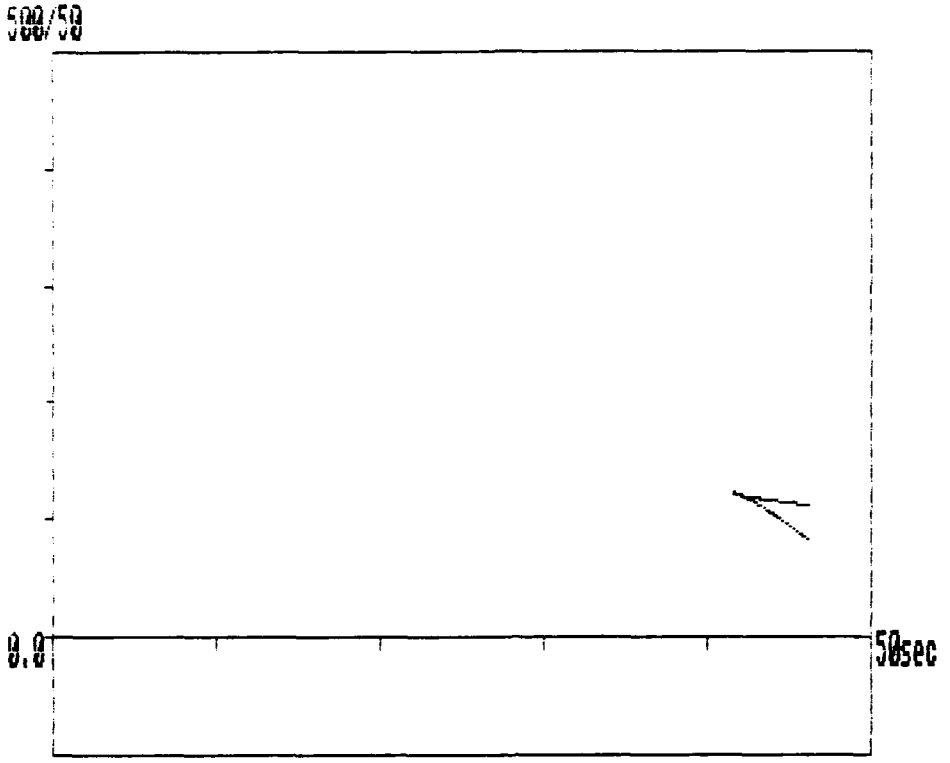

Figure 26: G256 Azimuth and Elevation Measurements for MLRS.

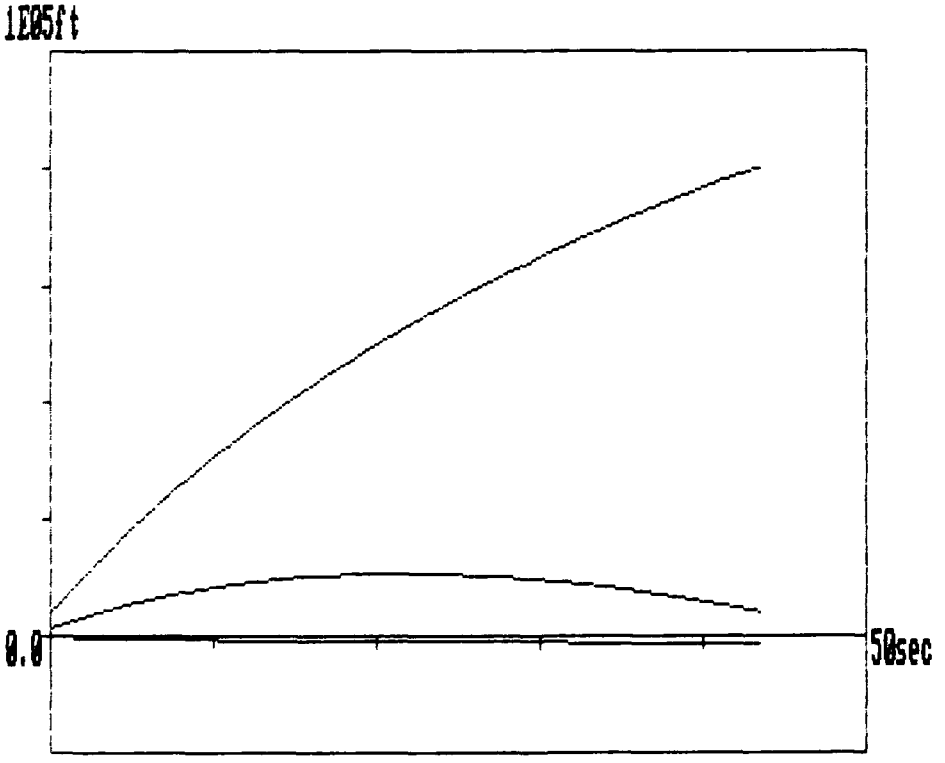

Figure 27: Derived Position Measurements from Radar #350.

An extended version of the DSRIF is needed since the nominal rocket trajectories were unavailable. The Extended DSRIF (E-DSRIF) may be derived by extending the observations equation, linearized about the current estimate, to

$$y_k^i = H_k^i x_k + v_k^i + z_k^i \tag{97}$$

where

$$z_k^i = h^i(x)\Big|_{x=x_k(-)} - H_k^i x_k(-) \tag{98}$$

and

$$H_k^i = \frac{\partial h^i(x)}{\partial x}\Bigg|_{x=x_k(-)} \tag{99}$$

and the dynamics equation, linearized about the current estimate, to

$$x_{k+1} = F_k x_k + B_k w_k + g_k \tag{100}$$

where

$$g_k = f(x)\Big|_{x=x_k(+)} - F_k x_k(+) \tag{101}$$

and

$$F_k = \frac{\partial f(x)}{\partial x}\Bigg|_{x=x_k(+)} \tag{102}$$

Substituting equations (97) and (100) into the least squares performance functional of equation (14) gives the following set of equations for updating the local filters in extended form:

Measurement Update

$${}_5T_k^i \begin{bmatrix} R_k^i(-) & z_k^i(-) \\ (R_k^i)^{-\frac{1}{2}} H_k^i & (R_k^i)^{-\frac{1}{2}} (y_k^i - z_k^i) \end{bmatrix} = \begin{bmatrix} R_k^i(+) & z_k^i(+) \\ 0 & e_k^i \end{bmatrix} \tag{103}$$

Time Update

$${}_6T_k^i \begin{bmatrix} R_w(k) & 0 & z_w(k) \\ -R_k^i(+)\, F_k^{-1} B_k & R_k^i(+)\, F_k^{-1} & (z_k^i(+) + R_k^i(+)\, F_k^{-1}\, g_k) \end{bmatrix}$$

$$= \begin{bmatrix} R_w^{*(i)}(k) & R_{wx}^{*(i)}(k) & z_w^{*(i)}(k) \\ 0 & R_{k+1}^{(i)}(-) & z_{k+1}^{(i)}(-) \end{bmatrix} \qquad (104)$$

Herein, ${}^5T_k^i$ and ${}^6T_k^i$ are orthogonal transformations which put the matrices on the left hand sides of (103) and (104) into upper triangular form (they may be implicitly computed using Householder transformations). All other variables are defined in the List of Symbols.

Processing on the global scale is the same as for the DSRIF i.e., the merge steps are exactly as defined in section 2.1. Only processing on the local scale is modified as such. A major difference between the E-DSRIF and DSRIF is that the local E-DSRIFilters require knowledge of the globally optimal estimate $x_k(\pm)$ in order to compute their first order Taylor series expansion terms F_k, g_k, H_k^i and z_k^i whereas the DSRIF may compute $x_k(\pm)$ at any rate less than the highest data rate. Future research should examine whether an E-DSRIF algorithm, in which the Taylor series expansions are about the locally optimal estimates, may be derived.

In order to derive a suitable dynamical model as well as initialize the filter, the position, velocity, acceleration and jerk of the rocket were precomputed using finite differencing with $\Delta t = .1$ seconds. Results are plotted in Figures 27 through 30 using all of the data provided for radar #350 except for the first 21 samples (we estimated that all rt's had locked onto the target by the 22nd sample). Figure 30 indicates that jerk is suitably modeled as a white Gaussia noise process with constant mean. Thus, the E-DSRIF was encoded in Fortran '77 using a second order polynomial dynamical model wherein

$$F_k = \begin{bmatrix} 1 & 0 & 0 & \Delta t & 0 & 0 & 0 & 0 & 0 \\ 0 & 1 & 0 & 0 & \Delta t & 0 & 0 & 0 & 0 \\ 0 & 0 & 1 & 0 & 0 & \Delta t & 0 & 0 & 0 \\ 0 & 0 & 0 & 1 & 0 & 0 & \Delta t & 0 & 0 \\ 0 & 0 & 0 & 0 & 1 & 0 & 0 & \Delta t & 0 \\ 0 & 0 & 0 & 0 & 0 & 1 & 0 & 0 & \Delta t \\ 0 & 0 & 0 & 0 & 0 & 0 & 1 & 0 & 0 \\ 0 & 0 & 0 & 0 & 0 & 0 & 0 & 1 & 0 \\ 0 & 0 & 0 & 0 & 0 & 0 & 0 & 0 & 1 \end{bmatrix}$$

and

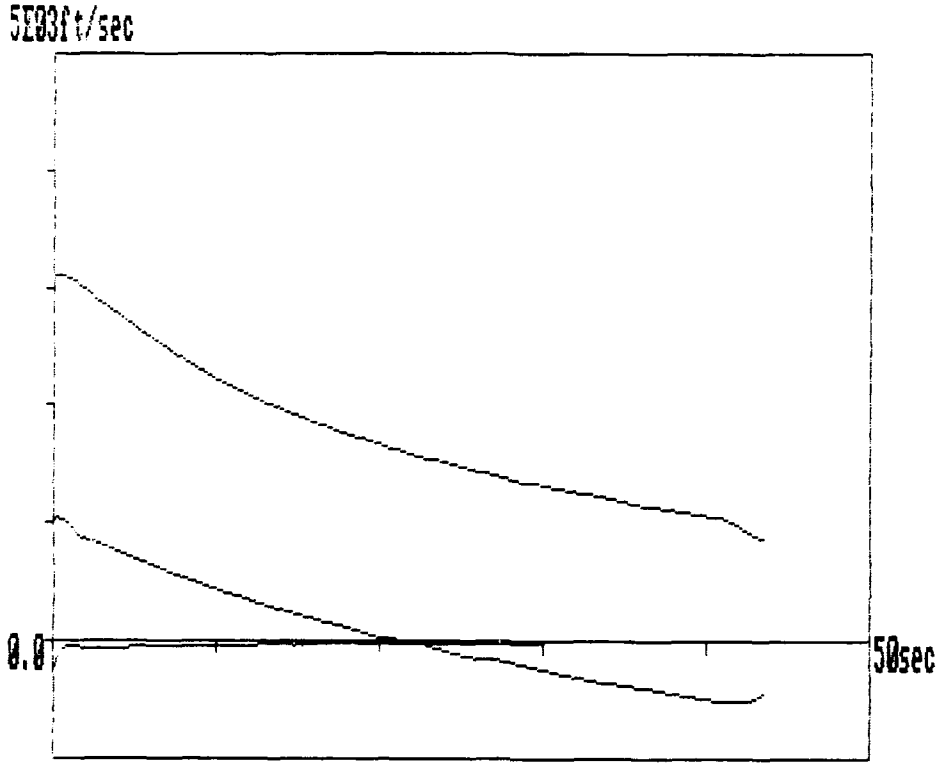

Figure 28: Derived Velocity Measurements from Radar #350.

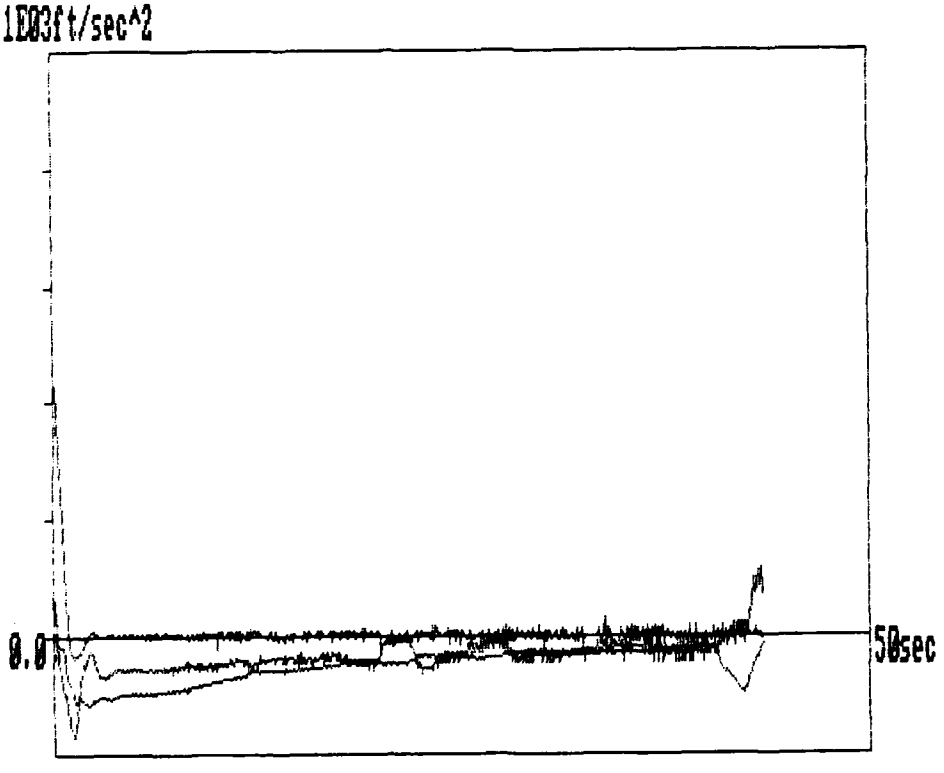

Figure 29: Derived Acceleration Measurements from Radar #350.

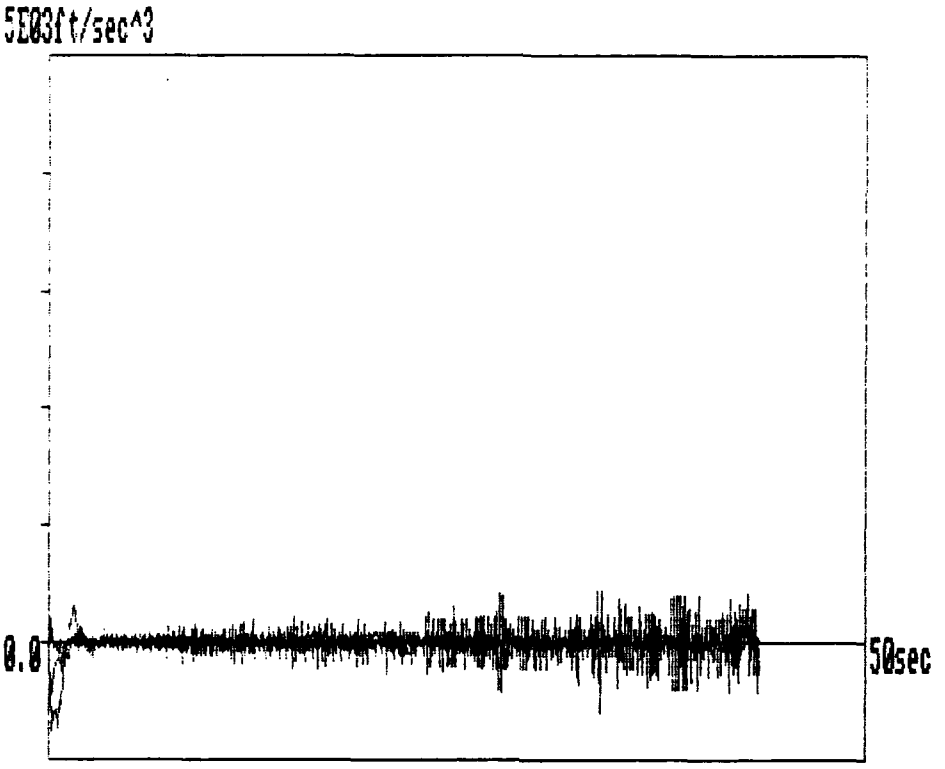

Figure 30: Derived Jerk Measurements from Radar #350.

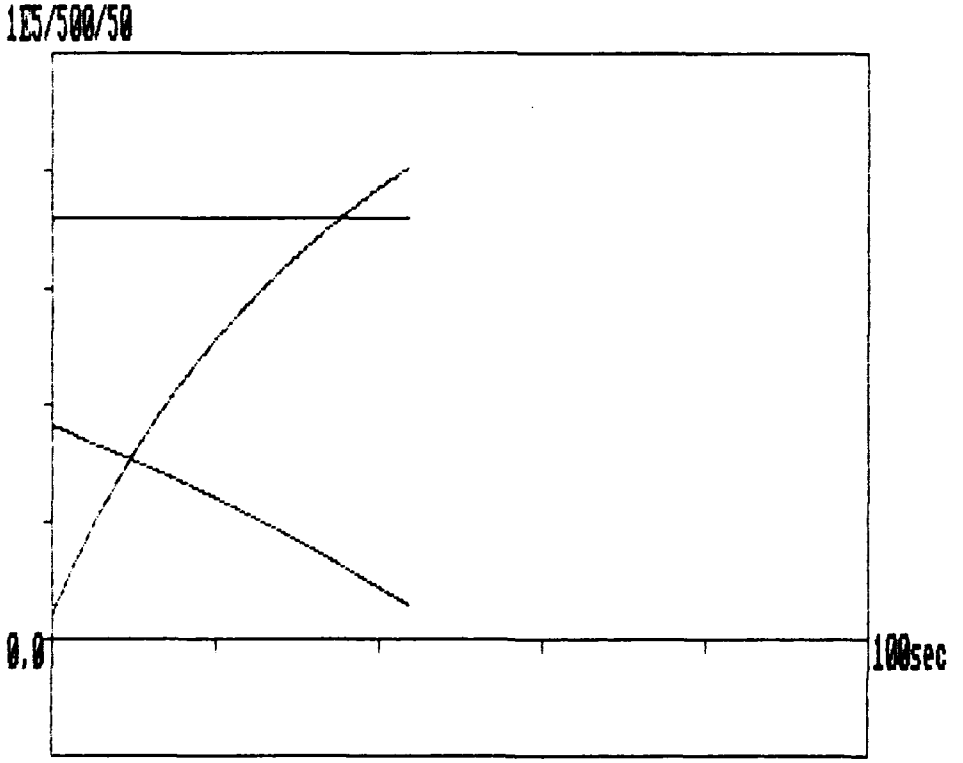

Figure 31: Radar #350 Range, Azimuth and Elevation Estimates for MLRS.
$R_k(j,j)=10^{10}$ for ot variables and 10.,1.,1. for rt range, azimuth and elevation variables respectively.
$Q_k(j,j)$ = diag [1.7×10^{17} 7.4×10^{17} 9.3×10^{17}] .

$$B_k = \begin{bmatrix} 0 & 0 & 0 \\ 0 & 0 & 0 \\ 0 & 0 & 0 \\ 0 & 0 & 0 \\ 0 & 0 & 0 \\ 0 & 0 & 0 \\ \Delta t & 0 & 0 \\ 0 & \Delta t & 0 \\ 0 & 0 & \Delta t \end{bmatrix}$$

The sample mean and covariace of w_k was computed to be

$$[\ -10.\ ft/sec^3 \quad -.055\ ft/sec^3 \quad -.48\ ft/sec^3\ ]$$

and

$$\text{diag}\ [\ 23{,}851.\ ft^2/sec^6 \quad 1{,}458.\ ft^2/sec^6 \quad 23{,}199.\ ft^2/sec^6\ ]$$

respectively. however, a much larger covariance was used in order to compensate for any errors in the model. Detailed testing of the algorithm is deferred to Phase II work wherein an adaptive method for adjusting Q_k in real time will be investigated.

Figures 31 through 35 show the rt and ot measurements as predicted by the E-DSRIF. Comparison with the actual measurements in Figures 16, 18, 19, 20 and 22 shows an exact match to within a plotting line width. A better means of comparison is thus provided below in Tables 5 and 6.

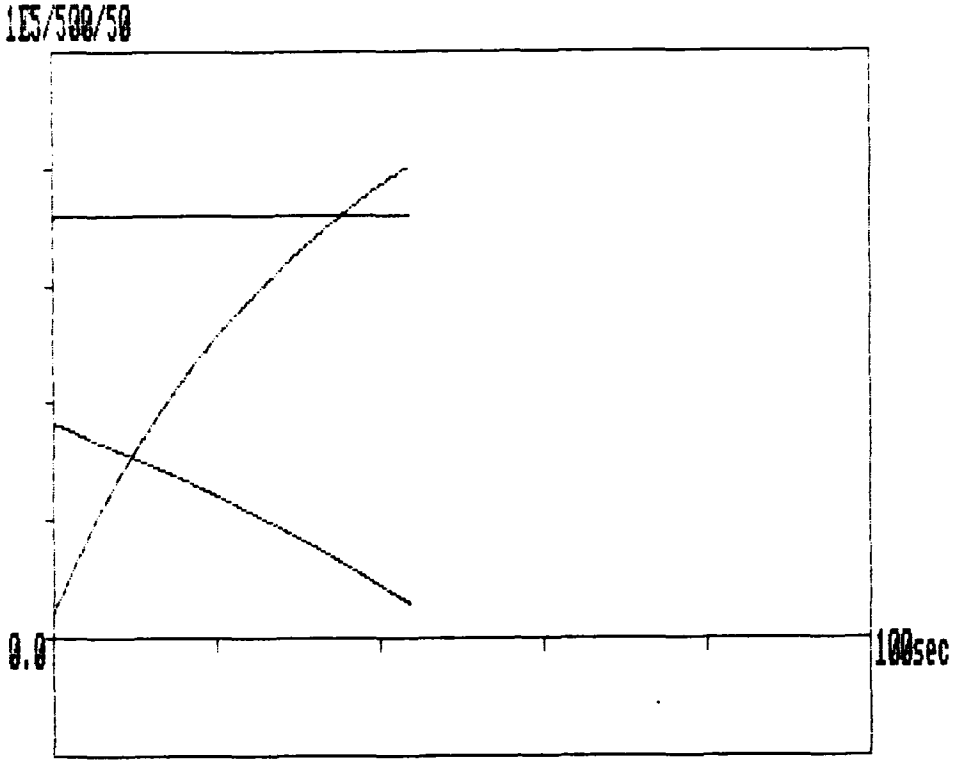

Figure 32: Radar #394 Range, Azimuth and Elevation Estimates for MLRS.
$R_k(j,j)=10^{10}$ for ot variables and 10.,1.,1. for rt range, azimuth and elevation variables respectively.
$Q_k(j,j)$ = diag [1.7×10^{17} 7.4×10^{17} 9.3×10^{17}] .

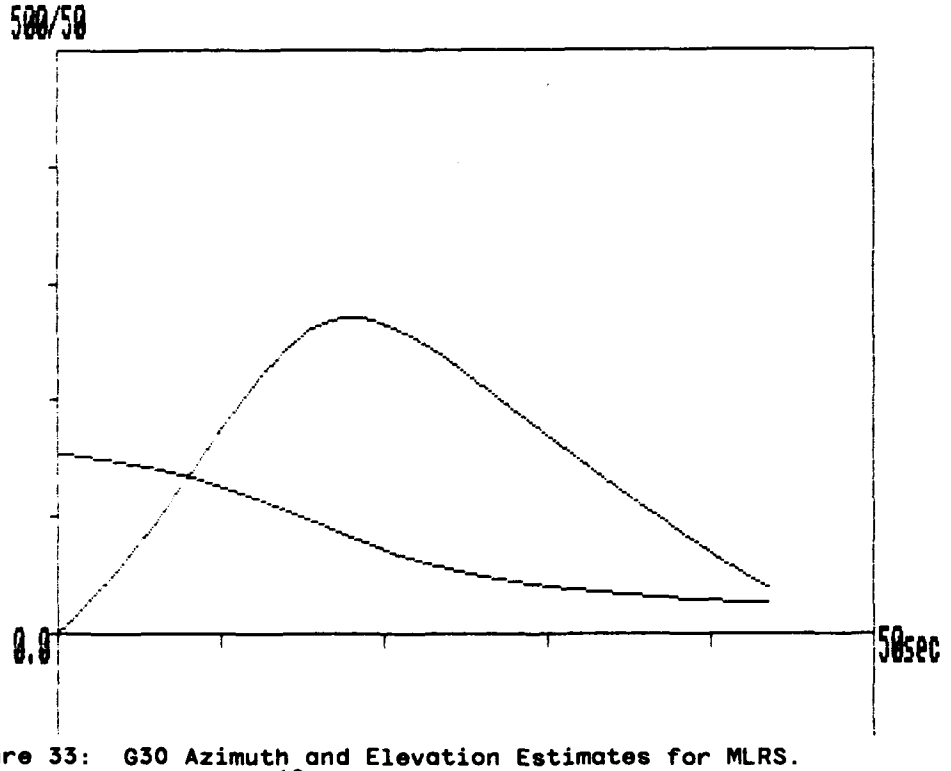

Figure 33: G30 Azimuth and Elevation Estimates for MLRS.
$R_k(j,j)=10^{10}$ for ot variables and 10.,1.,1. for rt range, azimuth and elevation variables respectively.
$Q_k(j,j)$ = diag [1.7×10^{17} 7.4×10^{17} 9.3×10^{17}] .

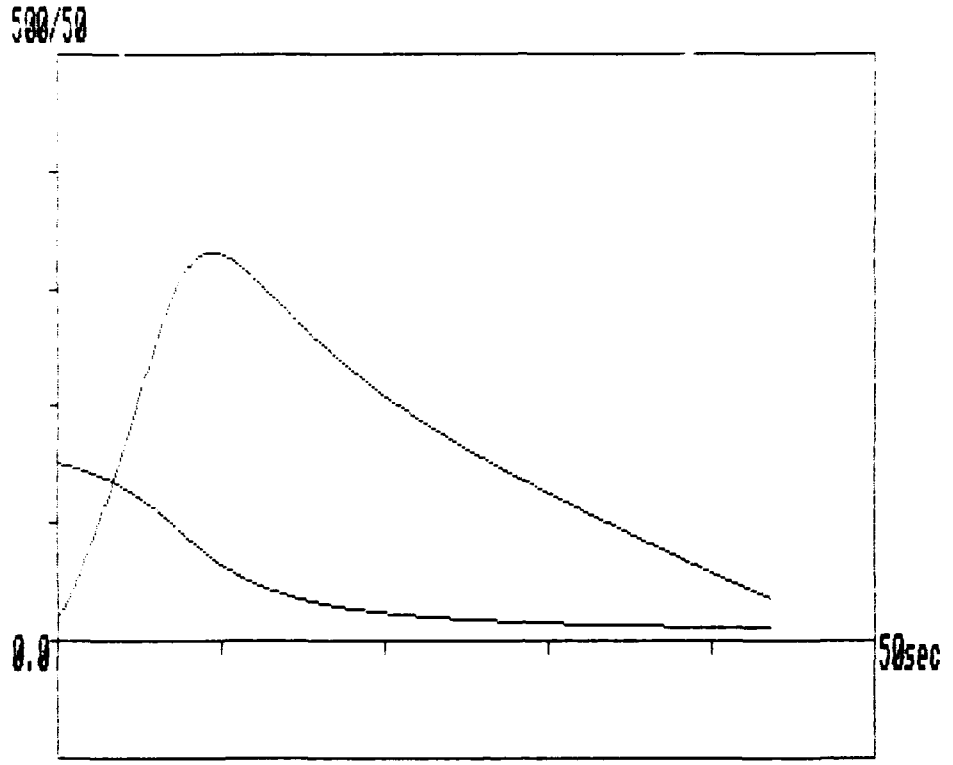

Figure 34: G80 Azimuth and Elevation Estimates for MLRS.
$R_k(j,j)=10^{10}$ for ot variables and 10.,1.,1. for rt range, azimuth and elevation variables respectively.
$Q_k(j,j)$ = diag [1.7×10^{17} 7.4×10^{17} 9.3×10^{17}] .

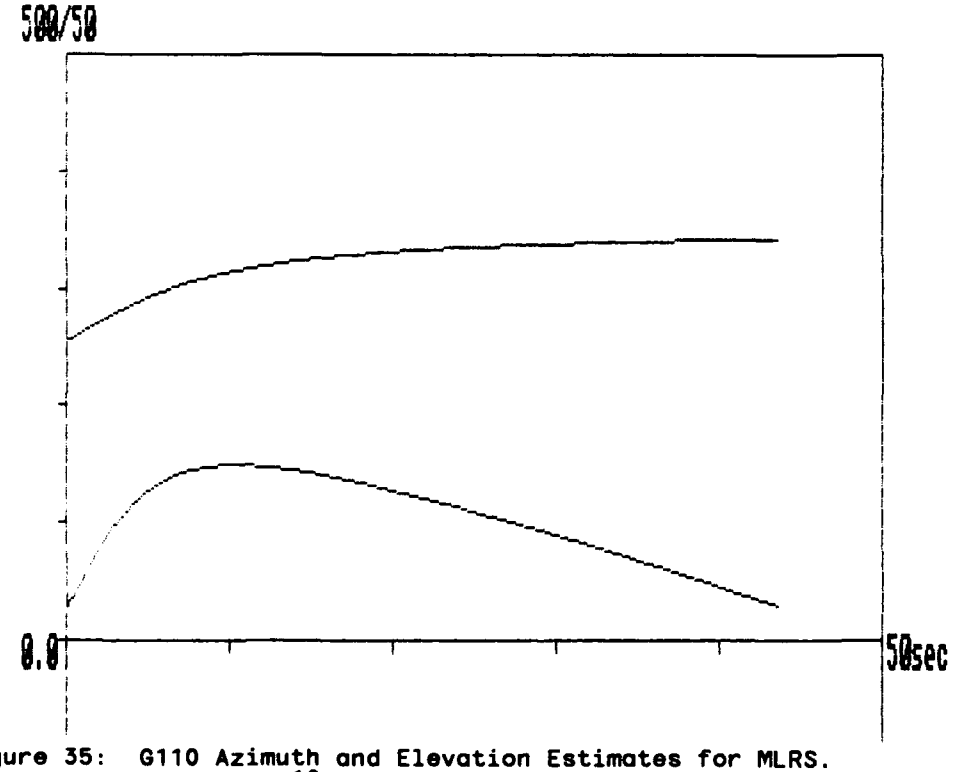

Figure 35: G110 Azimuth and Elevation Estimates for MLRS.
$R_k(j,j)=10^{10}$ for ot variables and 10.,1.,1. for rt range, azimuth and elevation variables respectively.
$Q_k(j,j)$ = diag [1.7×10^{17} 7.4×10^{17} 9.3×10^{17}] .

k	type	r_k^{12}	$\dot{r}_k^{12}$	θ_k^{12}	r_k^{14}	$\dot{r}_k^{14}$	θ_k^{14}
23	m	4,355.61	359.18	18.07	4,305.91	357.65	18.04
	e	4,355.61	359.19	18.74	4,355.61	359.19	18.74
24	m	4,683.17	358.91	18.07	4,665.94	358.30	18.09
	e	4,658.07	358.16	18.07	4,658.07	358.16	18.07
.							
.							
.							
229	m	52,171.33	358.96	11.88	52,163.32	358.95	11.89
	e	52,167.32	358.96	11.89	52,167.32	358.96	11.89
230	m	52,332.09	358.96	11.84	52,324.25	358.95	11.86
	e	52,328.15	358.96	11.85	52,328.15	358.96	11.85
.							
.							
.							
459	m	80,328.90	359.22	2.96	80,178.71	359.22	3.00
	e	80,254.10	359.22	2.98	80,254.10	359.22	2.98

Table 5: Radar #350 and #394 Measurements and Estimated Measurements for MLRS. $R_k(j,j)=10^{10}$ for ot variables and 10.,1.,1. for rt range, azimuth and elevation variables respectively.
$Q_k(j,j)$ = diag [1.7×10^{17} 7.4×10^{17} 9.3×10^{17}] .

k	type	r_k^3	θ_k^3	r_k^4	θ_k^4	r_k^1	θ_k^1
23	m	154.96	1.05	151.09	3.29	257.38	3.80
	e	154.97	.18	151.87	2.01	255.49	2.88
24	m	154.39	1.19	150.73	3.58	258.16	4.07
	e	154.90	.25	151.71	2.14	256.30	3.00
.							
.							
.							
229	m	68.57	28.54	22.78	21.75	***	***
	e	69.20	26.13	22.93	20.28	331.64	12.52
230	m	***	***	22.64	21.65	***	***
	e	68.74	26.07	22.80	20.18	331.73	12.48
.							
.							
.							
459	m	26.07	5.58	***	***	***	***
	e	26.32	3.94	10.98	3.66	342.28	2.98

Table 6: G30, G80, G110 Measurements and Estimated Measurements for MLRS. $R_k(j,j)=10^{10}$ for ot variables and 10.,1.,1. for rt range, azimuth and elevation variables respectively.
$Q_k(j,j) = \text{diag}\ [\ 1.7 \times 10^{17} \quad 7.4 \times 10^{17} \quad 9.3 \times 10^{17}\ ]$.
*** denotes data drop-out

The large values of Rk(j,j) for ot variables serves to weight the rt data much more heavily in computing estimates. Decreasing the ot measurement errors to more realistic values should give similar results since the predicted ot measurements matches their actual values very closely.

Figures 36 and 37 show the global position estimates and corresponding estimate error covariances respectively. Again, the rocket positions derived from radar #350 as compared with the E-DSRIF estimates based upon all of the 5 selected sensors, show extremely close agreement. The slight difference in the estimate of height is due to using $T^{launch} = I$ instead of its correct value as defined by equation (34). In Table 7 below, the estimates are compared using the correct cooordinate transformation.

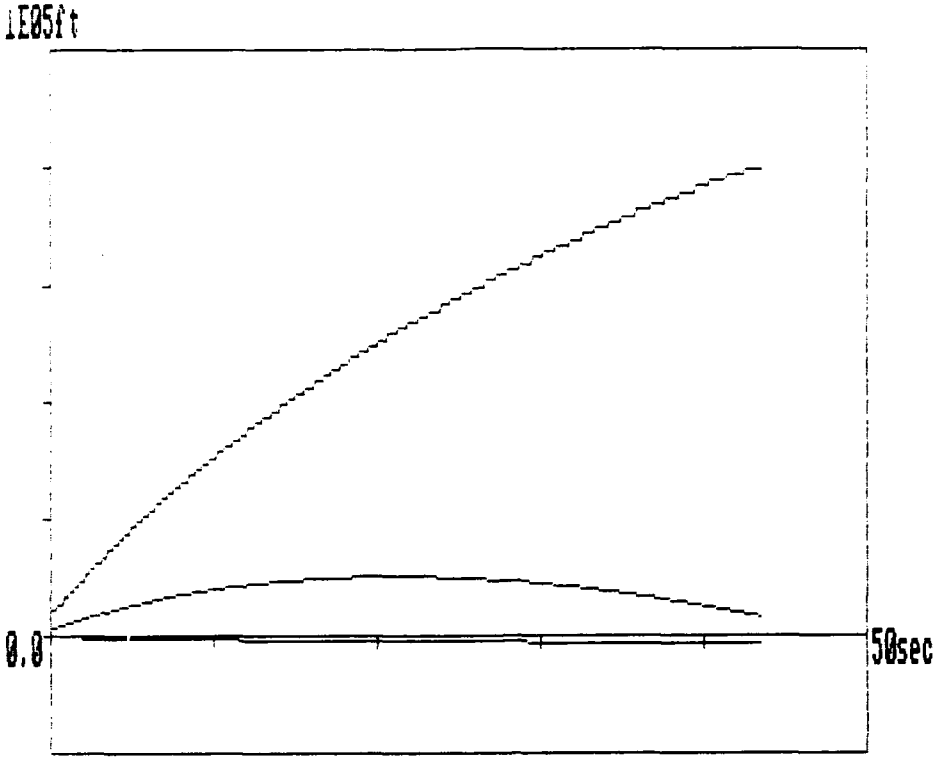

Figure 36: Global Position Estimates (w.r.t. launch) Versus Time for MLRS.
$R_k(j,j)=10^{10}$ for ot variables and 10.,1.,1. for rt range, azimuth and elevation variables respectively.
$Q_k(j,j)$ = diag [1.7×10^{17} 7.4×10^{17} 9.3×10^{17}] .

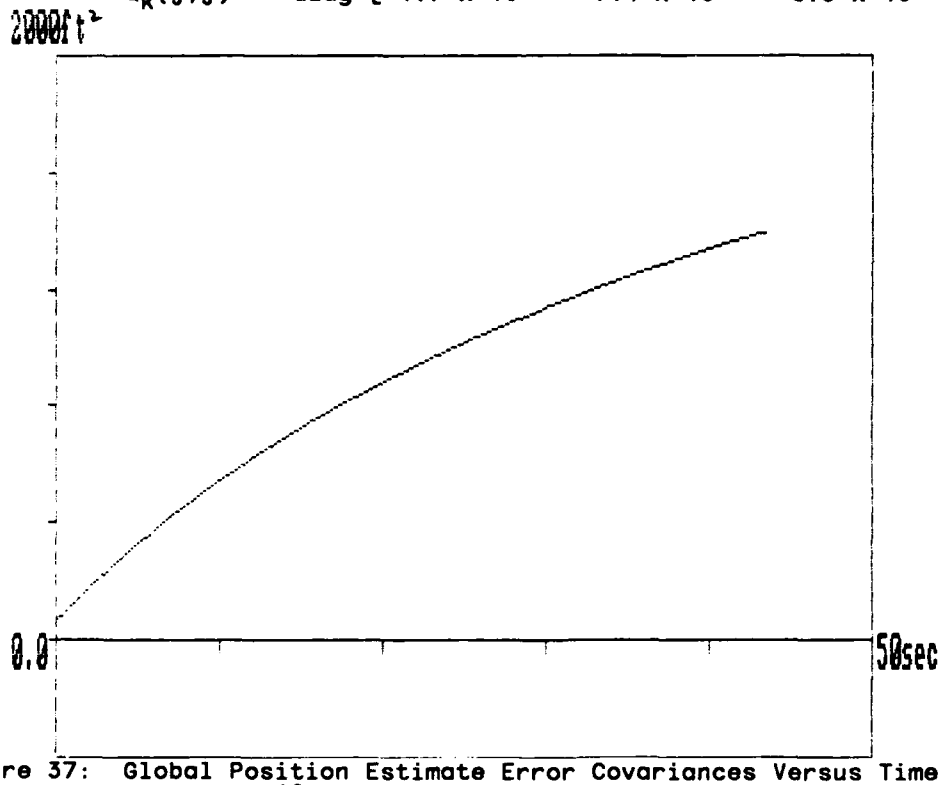

Figure 37: Global Position Estimate Error Covariances Versus Time for MLRS.
$R_k(j,j)=10^{10}$ for ot variables and 10.,1.,1. for rt range, azimuth and elevation variables respectively.
$Q_k(j,j)$ = diag [1.7×10^{17} 7.4×10^{17} 9.3×10^{17}] .

k	tp	x_k^1	x_k^2	x_k^3	x_k^4	x_k^5	x_k^6	x_k^7	x_k^8	x_k^9
22	e	-14,104.	-243,740.	3,754.	-296.	3,110.	1,015.	430.	-23.	73.
	m	..... same								
23	e	-14,189.	-243,437.	3,798.	-280.	3,104.	995.	429.	-23.	73.
	m	-14,076.	-243,413.	3,806.	-254.	3,120.	986.	436.	-23.	80.
24	e	-14,184.	-243,110.	3,903.	106.	3,271.	1,062.	497.	11.	85.
	m	-14,160.	-243,101.	3,905.	-211.	3,118.	994.	421.	-35.	49.
.										
.										
.										
229	e	-15,018.	-196,406.	12,646.	-19.	1,639.	1.	-.4	-45.	-15.
	m	-15,012.	-196,397.	12,641.	-17.	1,639.	-3.	1.6	-46.	-10.
230	e	-15,020.	-196,242.	12,646.	-20.	1,635.	-3.	-5.	-41.	-28.
	m	-15,014.	-196,233.	12,641.	-18.	1,635.	-4.	1.7	-49.	8.
.										
.										
.										
459	e	-15,197.	-167,388.	5,729.	22.	758.	-431.	21.	-221.	184.
	m	-15,202.	-167,307.	5,704.	8.	866.	-439.	.9	-25.	59.

Table 7: Global Position Estimates and Derived Measurements for MLRS. $R_k(j,j)=10^{10}$ for ot variables and 10.,1.,1. for rt range, azimuth and elevation variables respectively. $Q_k(j,j) = \text{diag}\ [\ 1.7 \times 10^{17} \quad 7.4 \times 10^{17} \quad 9.3 \times 10^{17}\ ]$.

Finally, the monotonically increasing estimate error covariance (actually, $P_0 = \text{diag}\ [\ 10^{12}\ ft^2 \ldots\ 10^{12}\ ft^2/sec^2 \ldots\ 10^{13}\ ft^2/sec^4 \ldots\ ]$ was used to initialize the covariance propagation so that the first step is a large, off scale decrease to approximately 100 ft^2) is due to our using values of Q_k approximately 12 orders of magnitude higher than its precomputed sample value. A more realistic value should result in a P_k with quite the opposite behavior.

3.0 Estimates of Technical Feasibility

The objective of Phase I research was to determine the feasibility of constructing an integrated test range tracking network based upon the DSRIF. A multitude of test range scenarios is envisioned so that a robust system is needed. At one extreme, test vehicles may include ballistic projectiles with well defined nominal trajectories a priori while at the other, multiple smart munitions with maneuvering capability is possible. The key to a successful network design is to employ a more or less sophisticated version of the algorithm depending upon the particular scenario. Thus the network must be adaptable. For example, preflight simulations of the proposed shot using high

fidelity aerodynamic models can yield good values for the process noise levels and a basic DSRIF should result in good tracking performance. However, a sudden departure from the nominal trajectory would require a detection mechanism as part of the algorithm and adjustment of Q_k in real time.

In order to determine the feasibility of our distributed approach to multisensor tracking, several specific technical objectives must be met. First and foremost, the basic DSRIF theory needs to be extended to enable the tracking of maneuvering vehicles, high dynamic trajectories, and multiple targets. The latter requires that a theory for associating data with targets, based upon the DSRIF, be developed. Other theoretical questions such as the development of a delayed-state DSRIF for processing range-rate measurements, a method for isolating faulty sensors, and efficient implementations of the DSRIF that facilitate high data rates need to be addressed.

Secondly, the DSRIF is a new algorithm which has undergone only limited testing in Phase I research. Extensive testing within a multisensor multitarget tracking scenario is needed. Finally, consideration needs to be given to the design of the tracking network both at the global and local levels. The major question here is whether a sufficient data rate can be achieved using current chip technology. Another question is whether the architecture can be reconfigured (in software) to implement other members of the family of DSRIFs. A DSRIF based multisensor laboratory tracking experiment should be performed.

For multitarget tracking, correlation of measurements with targets can best be done using a hypothesis testing approach. The idea is to select the correlation of measurements with targets that has maximum probability given the data. Calculation of all combinations to form the entire set of these conditional probabilities can be prohibiting, especially in a dense target environment. A major advantage in using the DSRIF is the tremendous reduction in computational cost associated with this calculation.

References

[1] Bierman, G.J. and M.R. Belzer, "A Decentralized Square Root Information Filter/Smoother," Proceedings of the 24th IEEE Conference on Decision and Control, pp. 1902-1905, 1985.

[2] Bierman, G.J., Factorized Methods for Discrete Sequential Estimation, Academic Press, New York, 1977.

[3] Wilsky, A.S., M.G. Bello, D.A. Castanon, B.C. Levy and G.C. Verghese, "Combining and Updating of Local Estimates and Regional Maps Along Sets of One-Dimensional Tracks," IEEE Transactions on Automatic Control, Vol. AC-27, No. 4, 1982.

[4] Athans, M., R. Wishner and A. Bertolini, "Suboptimal State Estimation for Continuous Time Nonlinear Systems from Discrete Noisy Measurements," IEEE Transactions on Automatic Control, Vol. AC-13, 1968.

[5] Wishner, R.P., J.A. Tabaczynski and M. Athans, "A Comparison of Three Nonlinear Filters," Automatica, Vol. 5, 1969.

[6] Alspack, D.L. and H.W. Sorenson, "Nonlinear Bayesian Estimation using Gaussian Sum Approximations," IEEE Transactions on Automatic Control, Vol. AC-17, 1972.

[7] Schwartz, L. and E.B. Stear, "A Computational Comparison of Several Nonlinear Filters," IEEE Transactions on Automatic Control, Vol. AC-13, 1968.